RESEARCH ARTICLE

Sono-exfoliated graphene-like activated carbon from hazelnut shells for flexible supercapacitors

Kiran Kumar Reddy Reddygunta[1] | Andrew Callander[2] | Lidija Šiller[3] |
Karen Faulds[2] | Leonard Berlouis[1] | Aruna Ivaturi[1]

[1]Smart Materials Research and Device
Technology (SMaRDT) Group,
Department of Pure and Applied
Chemistry, University of Strathclyde,
Glasgow, UK

[2]Centre for Molecular Nanometrology,
Department of Pure and Applied
Chemistry, Technology Innovation
Centre, University of Strathclyde,
Glasgow, UK

[3]School of Engineering, Newcastle
University, Newcastle upon Tyne, UK

Correspondence
Aruna Ivaturi, Smart Materials Research
and Device Technology (SMaRDT) Group,
Department of Pure and Applied
Chemistry, University of Strathclyde,
Thomas Graham Building, 295 Cathedral
Street, Glasgow, G1 1XL, UK.
Email: aruna.ivaturi@strath.ac.uk

Funding information
Defence Science and Technology
Laboratory; Engineering and Physical
Sciences Research Council, Grant/Award
Numbers: EP/P011500/1, NS/A000015/1;
Scottish Funding Council; University of
Strathclyde

Summary

Currently, more than 80% of commercial supercapacitors utilize chemically synthe-
sized carbon nanomaterials which are expensive and necessitates non-renewable
resources. Employing renewable, environment friendly and naturally available bio-
mass feedstock as precursor for producing carbon materials is a low-cost and sus-
tainable way for designing the electrodes of supercapacitors. In the present study,
high surface area hierarchical porous multilayered graphene-like carbon is
obtained via room temperature sono-exfoliation of the activated carbon synthesized
via simple and environmentally friendly hydrothermal carbonization and potas-
sium bicarbonate activation of waste hazelnut shells as the precursor. The high sur-
face area graphene-like carbon showed excellent electrochemical performance
with specific capacitance of 320.9 F g^{-1} at 0.2 A g^{-1} current density and exceptional
capacitance retention of 77.8% at 2 A g^{-1} current density after 10 000 cycles in 1 M
Na_2SO_4 electrolyte. Moreover, flexible supercapacitors fabricated using sono-
exfoliated graphene-like activated carbon coated stainless steel mesh electrodes and
biopolymer gel electrolyte exhibits an outstanding energy density of 38.7 W h kg^{-1}
and power density of 198.4 W kg^{-1}. These results show that mechanically exfoli-
ated graphene-like activated carbon derived from hazelnut shells exhibit superior
electrochemical performance that can compete with other activated carbon mate-
rials used in energy storage devices for real time applications.

KEYWORDS

activated carbon, biomass, bio-polymer electrolyte, flexible supercapacitor, graphene,
hazelnut shell, sono-exfoliation

1 | INTRODUCTION

Flexible supercapacitors are regarded as the "go to"
energy storage devices for portable and wearable elec-
tronics because of their ability to adapt to different wear
and tear environments without compromising their

electrochemical performance in addition to promising
features such as high energy/power density, longer life-
time and faster charge/discharge kinetics.[1,2] Carbona-
ceous materials such as carbon nanotubes and graphene
are the first choice for electrode materials in supercapaci-
tors because of their high chemical and mechanical

stability, extremely high specific surface area (SSA), and high electrical conductivity.[3,4] But from a sustainability point of view, these materials are not preferable as they utilize fossil fuels as their main precursors.[5] In recent years activated carbon developed from natural agricultural and forestry wastes has garnered much attention because of their rich availability in nature, as well as being cheap and renewable unlike fossil fuels.[6,7] Biomass derived activated carbon has unique features such as tuneable pore structures, high specific surface area, easily modified surface chemistry, excellent electrical conductivity, simple and cost effective preparation process, and are environmentally friendly.[8,9] Generally, the type of biomass carbon precursor and their inherent textural characteristics significantly impact the electrochemical properties of activated carbon electrodes. Over the last two decades, many biomass-derived activated carbon materials, particularly from nutshells, have shown promising electrochemical performance for energy storage applications, such as activated carbons derived from coconut shells,[10,11] palm kernel shells,[12] peanut shells,[13,14] walnut shells,[15] macadamia,[16] and pistachio shells[17] etc. Nut shells possess a high carbon and low ash content, hard texture and large micropore volume. Moreover, they are rich in lignin and cellulose which makes them promising feedstock for producing value-added porous activated carbon materials suitable for a diverse range of carbon-based applications.[18]

Corylus avellana, commonly known as hazelnuts or European hazel, are cultivated extensively in United States and European countries. They have significant commercial value in the food industry as a raw material for producing chocolate, nougat cookies, nut spreads, breakfast cereals and also in processed formulations such as hazelnut oil or praline paste.[19] Table 1 shows the chemical composition of hazelnut shells compared with other nut-shells. The chemical composition, which includes lignin, cellulose, and hemicellulose, is one of the crucial parameter to select the raw materials for activated carbon production. According to the previous studies on biomass activated carbon for supercapacitor application, high surface area carbonaceous materials are obtained from the

biomass with high percentage of lignin. It can be observed from Table 1 that hazelnut shells are rich in lignin and cellulose which makes them a suitable candidate for the production of high surface area activated carbon for supercapacitor applications. Moreover, hazelnut shells are the leftover by-products after hazelnut processing and have been traditionally considered to have little/no commercial significance. However, transforming these hazelnut shells into activated carbon could be beneficial owing to their high lignin and cellulose content. Activated carbon derived from hazelnut shells has been mainly studied for applications in CO_2 adsorption, as biosorbent for the recovery of Lithium, heavy metal ion adsorption, and more recently in supercapacitor electrodes.[20-22]

Theoretically, specific capacitance of biomass carbon electrodes is directly related to the pore structure and surface area of activated carbon electrode materials.[30] To achieve high specific surface area activated carbon from the biomass, in addition to the selection of precursor and activating agents, synthesis parameters such as impregnation ratio (biochar/ activating agent ratio), holding time (constant time at which the samples are annealed at a particular temperature), and holding temperature (constant temperature at which the samples are annealed for a constant time) play an important role. Suitable optimization needs to be carried out to obtain biomass activated carbon with a high specific surface area and pore volume which helps in enhancing energy storage. Traditionally, chemical activation is widely employed to obtain porous activated carbon material with well-defined pore size distribution. But the final products suffer from disordered carbon structures with large numbers of defects in the carbon framework. Hence, most of the time high temperature graphitization is used to obtain graphene-like activated carbon material with fewer defects and layered morphology. But these methods are neither economical nor scalable. In the present study, a particularly effective strategy of sono-exfoliation has been explored to solve these issues.

Because of its simplicity, low cost, and scalability, sono-exfoliation has gained renewed interest among academia and industry. Due to its high exfoliation efficiency, sono-exfoliation is regarded as an important method for

Biomass	Lignin	Cellulose	Hemicellulose	Ref
Palm shells	53.4	29.7	47.7	23
Peanut shells	26.4	40.5	14.7	24
Hazelnut shells	43.1	27.5	24.7	25
Walnut shells	48.1	23.9	22.2	26
Almond shells	29.54	38.48	29.54	27
Cashew nut shells	7.45	11.5	7.35	28
Macadamia nut shells	40.1	29.5	30.0	29

TABLE 1 Chemical composition of different types of nut shells

producing graphene via exfoliating graphite in liquid medium. The steps involved in the sono-exfoliation process are as follows: (1) dispersion of graphite in a solvent, (2) exfoliation using probe sonication, and (3) purification.[31] The use of an external driving force, such as ultrasonic waves, overcomes the Van der Waals interactions between the graphite layers, allowing the solvent molecules to intercalate.[32] Even though, sono-exfoliation is widely employed for producing high quality single or few layered graphene from bulk graphite, this method has been rarely explored for biomass activated carbon. Purkait et al. employed sono-exfoliation to create few layer graphene (FLG) sheets from peanut shells activated carbon for supercapacitor applications. As reported by them, the FLG material possessed a porous surface with profoundly broken sheet structures with high surface area ($2070 \ m^2 \ g^{-1}$) and excellent specific capacitance of $186 \ F \ g^{-1}$. Their research paved the way for synthesis of graphene like structures with high surface area and excellent electrochemical properties, from porous activated carbons.[13] Thus in the present study, room temperature sono-exfoliation is employed to produce high surface area porous activated carbon with graphene like structures from hazelnut shells.

Electrolytes also play a significant role in supercapacitors and it is imperative to use low cost, environmentally friendly electrolytes with high ionic conductivity, a wide voltage window, low flammability and volatility, good electrochemical and thermal stability.[33-35] A plethora of research has been reported on synthetic polymers (such as PVA, PEO, PAA, PMMA etc.) as the host polymer matrix to develop salt polymeric complex electrolytes.[36,37] However, even though synthetic polymers offer significant performance when used as electrolytes in supercapacitors, most of them are non-degradable materials. Whereas natural biopolymers such as chitosan, agar, and cellulose derivatives are biodegradable and have less/no impact on the environment since they are obtained from renewable resources.[38] Hence in the present study, hydroxyethyl cellulose (HEC) was employed as the host polymer network to accumulate ionic species as the gel electrolyte for solid-state supercapacitor applications. In the present study, sono-exfoliated graphene-like activated carbon derived from waste hazelnut shells has been used as an electroactive material and cellulose derivative based bio-polymer electrolyte as the ionic transport medium to fabricate flexible supercapacitors exhibiting excellent electrochemical performance with high specific capacitance as shown in Scheme 1.

2 | EXPERIMENTAL PROCEDURE

2.1 | Materials

The hazelnuts were purchased from a local super market and the nuts were separated from the shell. Potassium bicarbonate ($KHCO_3$), Sodium sulfate (Na_2SO_4), polyvinylidene fluoride (PVDF) binder, 1-methylpyrrolidine, sulfuric acid (H_2SO_4), Hydroxyethyl Cellulose (HEC) were obtained from Sigma-Aldrich. Hydrochloric acid was obtained from Fisher Scientific.
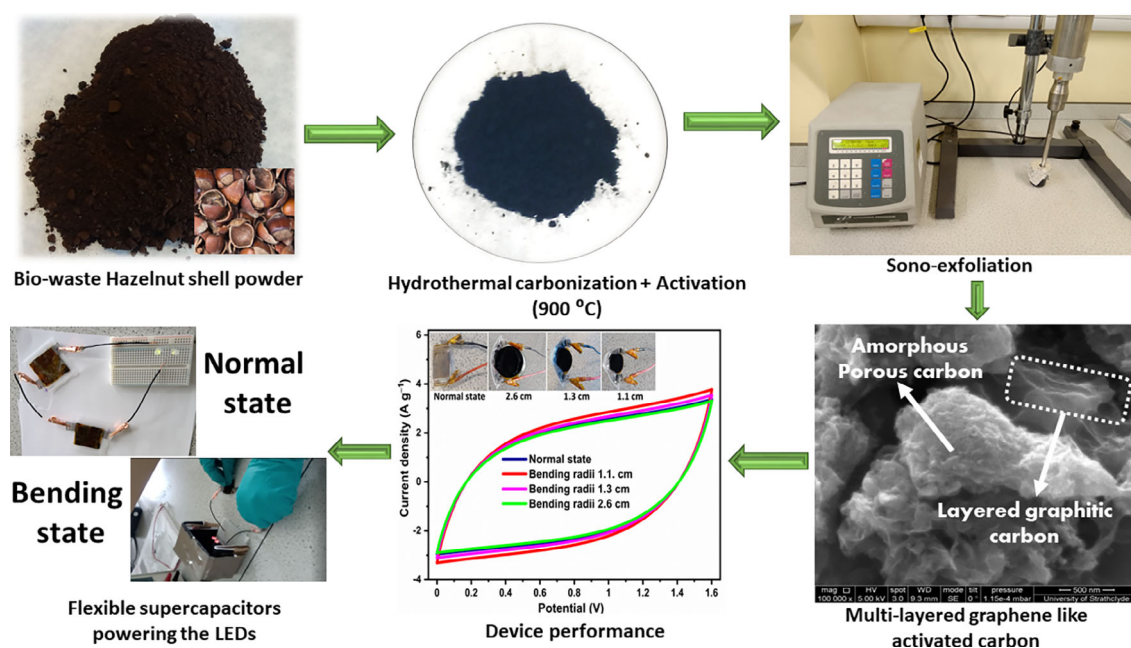
SCHEME 1 Schematic diagram showing the synthesis process along with the device performance

2.2 | Synthesis of activated carbon from hazelnut shells

2.2.1 | Hydrothermal carbonization and activation

Initially, the hazelnut shells were washed with deionized (DI) water, and then dried at 100°C for 24 h in hot air oven. The dried hazelnut shells were pulverized to powders using a Fritsch ball mill and sieved using a 100 μm mesh to collect fine powders of particle size ≤100 μm. 1.2 g of the obtained hazelnut shell powder was then mixed with 15 mL of distilled water and sonicated for 15 min. The mixture was then transferred into a 45 mL stainless steel autoclave and subjected to 180°C for 12 h. After 12 h, the autoclave was removed from the furnace and cooled down to room temperature. The resultant hydro char was filtered, washed with DI water and ethanol several times before drying at 80°C in a hot air oven.[39]

2.2.2 | Activation of hydrochar using different ratios of carbon to activating agent

For chemical activation at different ratios of Carbon: $KHCO_3$ agent, 1 g of hazelnut hydrochar was mixed with 1, 2, 3, or 4 g of $KHCO_3$ using a mortar and pestle. The mixture was then loaded into a ceramic boat and was placed at the center of a tube furnace. Each sample was activated for 2 h at 900°C. After 2 h, the furnace was switched off and allowed to cool naturally. The activated sample was taken out from the tube furnace and washed with 1 M HCl, ethanol, and DI water several times to remove any trace elements present in the sample until neutral pH was obtained.[40] The samples are termed as ACHS (1:1, 900, 2), ACHS (1:2, 900, 2), ACHS (1:3, 900, 2), and ACHS (1:4, 900, 2) respectively.

2.2.3 | Activation of Hydrochar under different holding temperatures

1 g of hazelnut hydrochar and 3 g of $KHCO_3$ (1:3 ratio of Precursor: Activating agent) was mixed using a mortar and pestle. The mixture was then activated at different temperatures [800, 900, and 1000°C] for 2 h. The furnace was then switched off and allowed to cool naturally. The activated sample was washed with 1 M HCl, ethanol, and DI water several times to remove any trace elements present in the sample until neutral pH was obtained. The sample was then dried at 80°C overnight in a hot air oven.[40] The samples are termed as ACHS (1:3, 800, 2), ACHS (1:3, 900, 2), and ACHS (1:3, 1000, 2) respectively.

2.2.4 | Activation of hydrochar under different holding times

1 g of hazelnut hydrochar and 3 g of $KHCO_3$ (1:3 ratio of Precursor: Activating agent) was mixed using a mortar and pestle. The mixture was then loaded into a ceramic boat and placed at the center of a tube furnace. The sample was activated for 1, 2, 3 h at 900°C. After the sample was activated for the specified time duration, the furnace was switched off and was allowed to cool naturally. The activated sample was then washed with 1 M HCl, ethanol, and DI water several times to remove any trace elements present in the sample until neutral pH was obtained.[40] The samples were termed as ACHS (1:3, 900, 1), ACHS (1:3, 900, 2), and ACHS (1:3, 900, 3) respectively.

2.2.5 | Sono-exfoliation of hazelnut shell derived activated carbon

The exfoliation of as obtained activated carbon ACHS (1:3, 900, 2) was performed in a 10% H_2SO_4 aqueous solution using a probe sonicator for 60 min with a pulse on-and-off time of 2 seconds. The sono-exfoliation process was carried out using Cole Palmer CPX750 model probe sonicator at an AC amplitude of 30% with a power of 750 W. The tip diameter used in this experiment was 6 mm, and it was dipped well into the solution but kept at least 1 cm distance from the bottom of the beaker containing the mixture. After 1 h, the final product was washed well with DI water until it reached pH 7 and dried at 90°C. For comparison purpose, ACHS (1:3, 900, 2) was also exfoliated under probe sonication for different time durations (30 min, 90 min, 120 min) and under different AC amplitudes (20% and 40%).

2.3 | Preparation of electrode material for electrochemical testing

Working electrodes were prepared by mixing Exf. ACHS (1:3, 900, 2) and PVDF (90:10 ratio of AC: binder) and ground in a mortar and pestle for 15 min. Once the mixture was thoroughly mixed, a few drops of NMP were added to prepare the slurry. The slurry was then coated on an area of 1 cm × 1 cm and 3 cm × 3 cm on stainless steel mesh using doctor blading. The 1 cm × 1 cm coated mesh electrode was used to study the electrochemical performance in aqueous electrolyte and 3 cm × 3 cm coated electrodes were used to fabricate solid-state flexible supercapacitor using gel electrolyte.

2.4 | Preparation of bio-polymer electrolyte

In this study, a hydroxyethyl cellulose (HEC) based salt-biopolymer complex was used as a gel electrolyte to fabricate flexible supercapacitor devices. Na_2SO_4 was used as the ionic salt to improve the ionic conductivity of the gel electrolyte. Typically, 2 g of HEC was dissolved in 20 mL of DI water at 90°C and stirred for 1 h. Next 2 g of Na_2SO_4 dissolved in 10 mL of DI water was added dropwise for 15 min to the solution and stirred at 90°C for another 1 h to produce a transparent HEC/Na_2SO_4 gel electrolyte. Before assembling the flexible supercapacitor device, the HEC/Na_2SO_4 gel electrolyte was coated on the surface of the 3 cm × 3 cm electrodes with graphene-like activated carbon and allowed to dry inside the fume hood at room temperature overnight. A white colored film/layer of HEC/Na_2SO_4 was formed on the surface of both the electrodes. The electrodes with the gel layer on the top were then carefully sandwiched without any separator and sealed tightly with vacuum sealer (soft vacuum mode). The sealed device was sealed tightly with a pellet press machine under an applied pressure of 1 ton for 5 min to improve the contact between the electrode and electrolyte interface.

2.5 | Material characterization

The specific surface area and pore volume of the as prepared samples were analysed via N_2 adsorption/desorption isotherm Brunauer-Emmett-Teller (BET) and Non-Linear-Density-Functional-theory (NLDFT) method using Micrometrics ASAP 2020 porosity analyser at 77 K. The crystallographic nature of the samples was examined by x-ray diffraction (XRD) using a Bruker D2 Phaser system using monochromatic CuK_α radiation with a wavelength of 1.5406 Å. The samples were scanned in the range 5–80° and an increment of 0.04 on the 2θ scale. The substrates were set to a rotation speed of 8 per min throughout the measurements. The morphological features were obtained using FEI Quanta 250 FEGSEM using 5 kV electron beam. EDX spectra were acquired from the full area of the corresponding 1000 × magnification image using a 20 kV electron beam. Transmission electroscope microscope (TEM) images were obtained using a JOEL 2100F FEG TEM operated with an accelerating voltage of 200 kV. The interlayer spacing between graphitic carbon layers was calculated using imagej software. TGA analysis was carried out using Perkin Elmer TGA 7 apparatus under inert Ar atmosphere. FTIR analysis was performed using Perkin Elmer FTIR sub tech within a spectral range of 500 to 3500 cm^{-1}. The mass loss as a function of temperature was measured between 40 and

900°C at 10°C/min heating rate. X-ray photoemission spectroscopy (XPS) analysis was conducted using a Thermo Scientific K-alpha X-ray Photoelectron Spectrometer (Thermo Scientific, East Grinstead, UK). High resolution photoemission spectra of specific element regions (C1s, O1s, N1s) were collected at 40 eV pass energy of hemispherical electron analyser with 0.05 eV energy step size. Spectra were acquired using a monochromatic Al K_α x-ray source with an output energy of 1486.6 eV with a maximum x-ray beam spot size of 400 μm. Surface charge compensation was obtained with a low energy dual-beam electron/ion flood gun. Raman spectra were measured using a WiTec Raman microscope with an excitation wavelength of 532 nm within a spectral range of 500 to 3500 cm^{-1}, to study the defective/graphitic nature of the as prepared samples. The laser power was set to 14.92 mW after using 10X objective lens with an acquisition time of 10 s. Calibration was performed using a silicon standard (520 cm^{-1}). Samples were analysed under the microscope and five different spectra were recorded from different parts of the sample, and averaged to gain a representative spectrum using MATLAB script. All spectra were normalized and Voigt fitting was used for the devolution of the spectra with Fityk software.

2.6 | Electrical conductivity and Electrochemical measurements

The DC electrical conductivity of powdered ACHS (1:3, 900, 2) and Exf. ACHS (1:3, 900, 2) samples are measured using Linear Sweep Voltammetry (LSV) technique. The samples were made into pellets by mixing 30 mg of Exf. ACHS (1:3, 900, 2) and 3 mg of PVDF (90:10 ratio of AC: binder) thoroughly in a mortar and pestle for 15 min. Once the mixture was thoroughly mixed, the powder was transferred into a circular pellet dyes which is then pressed tightly using laboratory pellet press machine under 10 tons pressure for 10 min. The pellets are then carefully separated from the pellet dye and cut into rectangular shaped pellets (L × w × t = 1.2 cm × 1 cm × 0.49 mm) as shown in Figure S4A (Supporting information). Two-probe method was used to measure the conductivity of obtained pellets. LSV was carried out at room temperature using an Autolab PGSTAT 302 N potentiostat/galvanostat with FRA32M module. The electrical conductivity of the powder samples was estimated by means of Equation (1)[41]:

$$\sigma = \frac{I}{V} \times \frac{t}{A} = \frac{1}{R} \times \frac{t}{W \times L},$$ (1)

where the Resistance (R) was obtained by fitting the linear region of current-voltage (I-V) curve to Ohm's law, L is the pellet length, w is the pellet width, and t is the

thickness of the pellet placed between the two current collectors (Copper tape in this case).

Three electrode and flexible symmetric two electrode configurations were employed to investigate the electro-chemical properties of the as-prepared activated carbon coated stainless steel electrodes. Cyclic Voltammetry (CV), galvanostatic charge-discharge (GCD), and electro-chemical impedance spectroscopy (EIS) analysis were carried out at room temperature using an Autolab PGSTAT 302 N potentiostat/galvanostat with FRA32M module. For a typical three electrode configuration, activated carbon coated stainless steel electrode, Ag/AgCl, and Platinum rod were used as the working, reference, and counter electrodes, respectively, and 1 M Na_2SO_4 in DI water was employed as the electrolyte.

The specific capacitance C_s (Farad/g) was estimated from galvanostatic charge-discharge measurements in three electrode configuration by means of Equation (2)[42]:

$$C_s = \frac{I \times \Delta t}{m\Delta V},\tag{2}$$

where I represent the current (in ampere), Δt is the discharge time, m is the mass of the active material on the electrode, and ΔV is the potential window.

The energy density is an important performance evaluation parameter and estimated using Equation (3)[43]:

$$E_d = \frac{1}{2}\frac{C_s \times \Delta V^2}{3.6}.\tag{3}$$

Power density is another important parameter extensively used to study the supercapacitor performance and is given by Equation (4)[43]:

$$P_d = \frac{E_d \times 3600}{\Delta t}.\tag{4}$$

The flexible supercapacitor device with HEC/Na_2SO_4 electrolyte was subjected to electrochemical tests using a two-electrode configuration to evaluate its performance. The performance evaluation parameters, electrode specific capacitance C_{es} (F g^{-1}), total capacitance (C_t) of the device, energy density (Wh kg^{-1}) and power density (W kg^{-1}), were estimated from galvanostatic charge-discharge measurements in a two electrode configuration by means of the following Equations.[44]:

$$C_t = \frac{I \times \Delta t}{M\Delta V},\tag{5}$$

$$C_{es} = 4 \times C_t,\tag{6}$$

$$E = \frac{1}{2}\frac{C_t \times \Delta V^2}{3.6},\tag{7}$$

$$P = \frac{E_d \times 3600}{\Delta t},\tag{8}$$

where I represent the current (in ampere), Δt is the discharge time, M is the total weight of active material within the two electrodes, and ΔV is the potential window.

3 | RESULTS AND DISCUSSIONS

In this study a two-stage hydrothermal carbonization (HTC) and potassium bicarbonate activation was used for the synthesis of high surface area porous activated carbon from hazelnut shells. Before the hydrothermal carbonization and activation process was performed, the composition and thermal degradation of hazelnut shell powder was characterized using CHN elemental analysis and Thermogravimetric analysis (TGA) respectively. According to elemental analysis, the carbon, hydrogen, nitrogen, and oxygen content in the hazelnut shell powder was found to be 51.19%, 5.36%, 0.35%, and 43.1%, respectively, which is similar to the value reported in the literature. Yuksel et al. studied the valorization of hazelnut shell waste in hot compressed water where they reported carbon, hydrogen, nitrogen, and oxygen content of 50.44%, 6.76%, 0.76%, and 41.92% respectively.[45] Figure S1A (Supporting information) shows the thermogravimetric analysis (TGA) of raw hazelnut shell powder. The lignin, cellulose, and hemicellulose that make up the hazelnut shell degrade at different temperatures due to the differences in their structure and composition. As shows in Figure S1A, the pyrolysis of hazelnut shell powder occurs in three stages. The release of moisture in hazelnut shell powder causes a slight initial weight loss of 7.6% between 40 and 180°C, corresponding to first stage of breakdown. The second stage of volatization is called the active pyrolysis area which is divided into two phases between 200 and 520°C corresponding to the decomposition of hemicellulose and cellulose. The thermal decomposition of hemicellulose begins exactly after 200°C with a weight loss of 38% indicating the decomposition of hemicellulose. And in temperatures between 330 and 520°C, a weight loss of 29% is observed, indicating the breakdown of cellulose. According to literature, the decomposition of cellulose and hemicellulose for various biomass samples occurs between 215–400°C.[46,47] But from the graph, it can be observed that there is a significant shift in peaks toward higher temperature due to the strong

intramolecular forces present between cellulose and hemicellulose molecules. The decomposition of lignin varies over a wide range of temperature from 520 to 900°C which is indicated by long tail after 520°C. This area is called the passive area where the degradation occurs very slowly leaving behind 19.56% of lignin-rich carbonaceous biochar at 900°C. Thus, TGA gives important information on the temperature regions one could explore for producing the activated carbon. Nonetheless, TGA data cannot be solely considered for setting up the activation temperature because removing the volatile fraction from pores requires a significantly higher temperature (over 700°C). Moreover, carbonaceous materials with high specific surface area and pore-volume have been reported to be obtained if the activation process was carried out at temperatures greater than 700°C.[48] Hence, in this present study, the starting temperature for potassium bicarbonate activation was chosen to be 800°C which is then followed by the optimization process with respect to holding temperature, impregnation ratio, and holding time.

Surface area, pore volume, and degree of graphitization of the samples was tuned by varying the hydrochar to $KHCO_3$ ratio, holding time and holding temperature. The samples are termed as ACHS followed by the corresponding impregnation ratio, holding temperature and holding time in brackets. Furthermore, sono-exfoliation of activated carbon was performed to enhance the surface area and degree of graphitization. The mechanically exfoliated samples are termed as Exf. ACHS (mentioned along with the impregnation ratio, holding temperature, and holding time). The effect of synthesis parameters on the surface area and structural properties of the as-obtained samples was studied using N_2 adsorption/desorption isotherms, X-ray diffraction (XRD), and Raman spectroscopy. The compositional, structural, and morphological features of the optimized samples were studied using X-ray photoelectron spectroscopy (XPS), Field Emission Scanning Electron Microscopy (FESEM), and High-Resolution Transmission Electron Microscopy (HRTEM). Furthermore, the electrochemical performance of the various activated carbon samples was investigated and compared in a 3-electrode configuration using 1 M Na_2SO_4 electrolyte using cyclic voltammetry (CV), galvanostatic charge discharge (GCD), and electrochemical impedance spectroscopy (EIS). The feasibility of the sono-exfoliated sample for the real time practical application was studied by fabricating flexible supercapacitors using the bio-polymer (hydroxyethyl cellulose/Na_2SO_4) electrolyte. Experimental section gives the details of the methodology used for material synthesis, electrolyte, and electrode formation and device fabrication and characterization.

3.1 | N_2 adsorption/desorption isotherms

Figure 1 shows the N_2 absorption/desorption isotherms and pore size distribution plots of the activated carbon samples produced under different experimental conditions (impregnation ratio, holding time, holding temperature, and sono-exfoliation). Table 2 gives the corresponding estimated values of the specific surface area and pore volume for each of the samples. Nearly all the isotherms resemble type IV curves according to IUPAC classification models, manifesting interconnected micro/mesoporous network.[49] The hysteresis curves with H4 loop is observed in the relative pressure region of 0.4 to 0.9 P/P_0 which indicates that capillary condensation occurs in the mesopores.[50] The sharp rise in the adsorption isotherm at low relative pressures that is, below 0.4 P/P_0 is attributed to micropores. Hence, it can be concluded that the resulting samples were mainly composed of micro/meso porous structures which is beneficial for charge transfer and storage. Pore size distribution plots suggest the presence of mesopores sizes in the 2-5 nm range (the highlighted region). Hence, even though the pore size is around 2-5 nm in all ACHS samples, their average pore volume varies drastically as shown in Table 2. The mechanically exfoliated sample possesses the highest pore volume of 1.87 cm^3g^{-1} which suggests that the sono-exfoliation not only separated the graphene-like layers, but also corroded the carbon surface further thus enhancing the pore volume and surface area.[13]

3.1.1 | Effect of impregnation ratio (Carbon: $KHCO_3$ ratio)

The effect of varying the amount of activating agent on the textural properties of the activated carbon prepared at holding temperature of 900°C for 2 h was investigated and the results are summarized in Table 2. It can be observed that the BET surface area and pore volume increased from 857 to 2112 $m^2 g^{-1}$ and from 0.57 to 1.57 $cm^3 g^{-1}$, respectively, as the impregnation ratio increased from 1:1 to 1:3. Further increasing the impregnation ratio to 1:4 resulted in a decrease in both the specific surface area and pore volume to 1782 $m^2 g^{-1}$ and 1.13 $cm^3 g^{-1}$ respectively. These experimental results reveal that a higher impregnation ratio not only created/added new pores but also enlarged the existing pores, ultimately leading to structural contraction and collapse of the pores. A similar, increase in the specific surface area from 1243 $m^2 g^{-1}$ to 1642 $m^2 g^{-1}$ was reported for activated carbon derived from hazelnut shells when the biochar: KOH content was increased from 1:1 to 1:3.[51] In
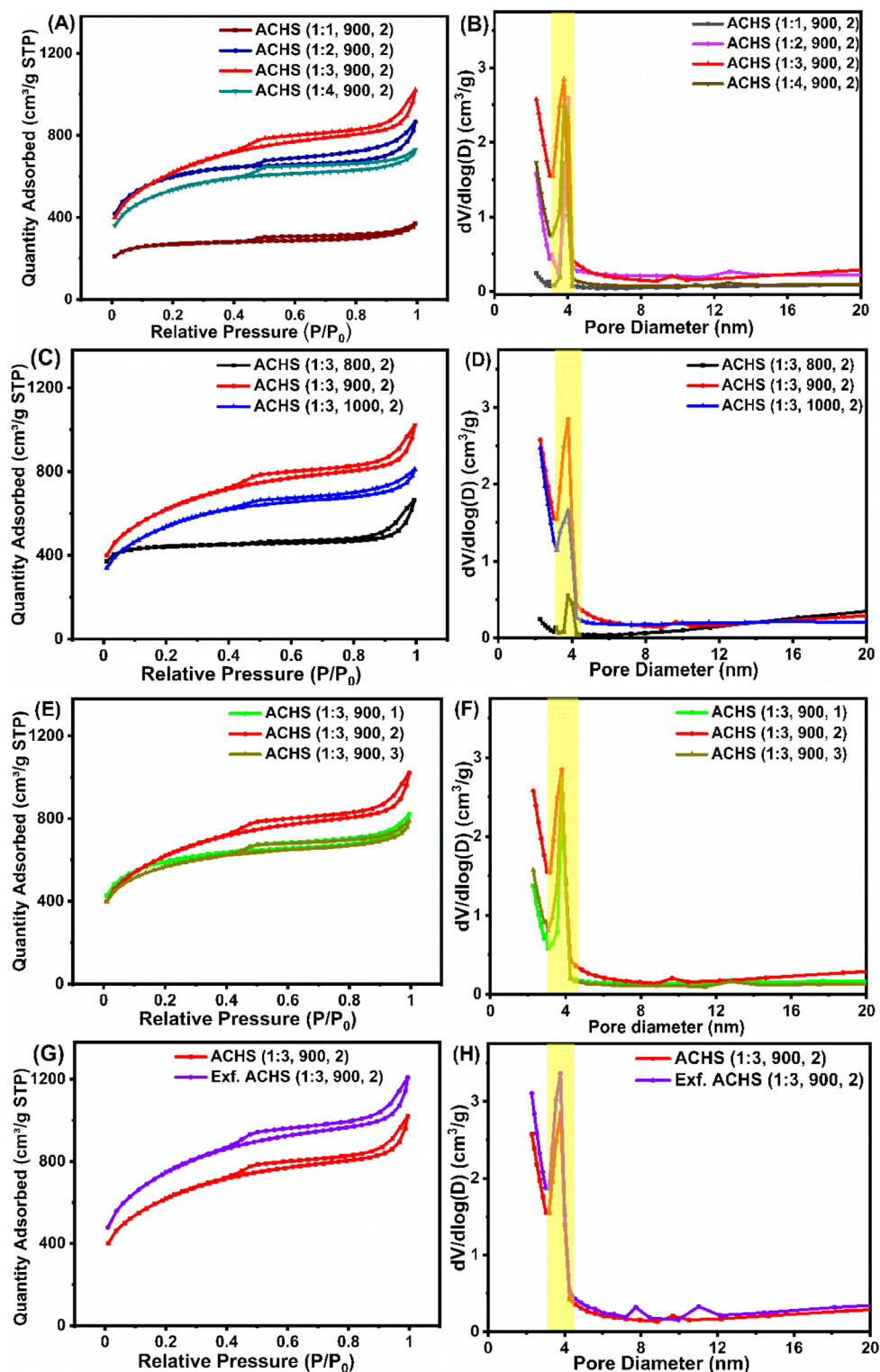
FIGURE 1 N_2 absorption/desorption isotherms and pore size distribution data of activated carbon produced using different (A and B) impregnation ratios (C and D) holding temperatures (E and F) holding times (G and H) Activated carbon sample ACHS (1:3, 900, 2) before and after exfoliation. Pore size distribution plots suggests the presence of mesopores centered around 2-5 nm range (the highlighted region). The as-synthesized activated carbon samples are termed as ACHS whereas the sono-exfoliated samples are termed as Exf. ACHS and are mentioned along the corresponding impregnation ratio (Carbon: $KHCO_3$), holding temperature ($°C$), and holding time (h) in brackets

another study, the surface area of activated carbon prepared from α-D glucose using potassium bicarbonate as activating agent was reported to decrease from 2230 to 2000 $m^2\ g^{-1}$ when the impregnation ratio increased from 1:6 to 1:8.[40] These results show that activated carbon formed with an optimal impregnation ratio of 1:3, at a holding temperature of 900°C and a holding time of 2 h showed maximum surface and pore volume, indicating a larger number of active sites for charge/ions storage at the electrode/electrolyte interface.

3.1.2 | Effect of holding temperature

As indicated in Table 2, the surface area and pore volume increased as the holding temperature increased from

TABLE 2 Textural properties of the as-prepared samples. The as-synthesized activated carbon samples are termed as ACHS whereas the sono-exfoliated samples are termed as Exf. ACHS and are mentioned along the corresponding impregnation ratio (Carbon: $KHCO_3$), holding temperature (°C) and holding time (h) in brackets

Sample ID	Specific surface area ($m^2 \, g^{-1}$)	Pore volume ($cm^3 \, g^{-1}$)
ACHS (1:1, 900, 2)	857	0.57
ACHS (1:2, 900, 2)	1965	1.33
ACHS (1:3, 900, 2)	2112	1.57
ACHS (1:4, 900, 2)	1782	1.13
ACHS (1:3, 800, 2)	1383	1.02
ACHS (1:3, 1000, 2)	1838	1.25
ACHS (1:3, 900, 1)	1929	1.27
ACHS (1:3, 900, 3)	1868	1.21
Exf. ACHS (1:3, 900, 2)	2545	1.87

800 to 900°C but followed a downward trend when temperature was increased further to 1000°C. A maximum surface area of 2112 $m^2 \, g^{-1}$, with pore volume of 1.57 $cm^3 \, g^{-1}$, was obtained for the sample prepared at a holding temperature of 900°C. These results indicate an enhancement of the pore network with increase in holding temperature until 900°C, above which the network began to break down resulting in a decrease in surface area and pore volume for the sample prepared at a holding temperature of 1000°C. A similar type of phenomena was reported for activated carbon derived from spruce bark, where the surface area decreased from 2385 to 2155 $m^2 \, g^{-1}$ resulting from a collapse of porosity when the temperature was increased from 900 to 1000°C.[39]

3.1.3 | Effect of holding time

The data in Table 2 show that with the increasing holding time, the surface area and pore volume of activated carbon first increased when the holding time was increased from 1 to 2 h, but then decreased for longer times. At a holding temperature of 900°C and a holding time of 2 h, the surface area and pore volume reached a peak value of 2112 $m^2 g^{-1}$ and 1.57 $cm^3 \, g^{-1}$ respectively. This would suggest that during the first hour at that temperature the formation of pores is initiated within the carbon framework whereas during the next hour, further etching/expansion of the pore network occurred thereby increasing the surface area and pore volume. A further increase in the holding time to 3 h, led to a decrease in the pore volume due to the shrinkage in pore network.

Indeed, longer holding times at higher temperatures leads to more damage to the porous framework. Hence, an optimal temperature holding time of 2 h was selected for further work in order to produce activated carbon with a high surface area and pore volume.

3.1.4 | Effect of sono-exfoliation

The effect of mechanical exfoliation on the surface area and pore volume is also revealed in Table 2. As noted above, carefully designed layered carbonaceous materials with good micro/meso porous framework is highly desirable for supercapacitors with high energy and power density. Materials with a high specific area and pore volume can accumulate sufficient charge carriers (resulting in high energy density) and provide faster charge transport kinetics (resulting in high power density) which are essential for electrochemical supercapacitor applications.[8,49,52] In order to optimize these properties, the specific surface area and pore volume of activated carbon samples produced from chemical activation can be further improved by a simple sono-exfoliation process using probe sonication. It is evident from the data in Table 2 that, sono-exfoliation not only improves the porosity of the chemically activated samples but also reduces the number of defects in the carbon framework, as also verified by from the Raman spectra (discuss below). Exfoliation increased the surface area from 2112 to 2545 $m^2 \, g^{-1}$ with a high pore volume of 1.87 $cm^3 \, g^{-1}$ leading to more active surface sites that are accessible to the electrolyte ions. Recently, in-situ ultra-high-speed optical imaging studies and acoustic field pressure measurements were performed to gain new insights into the sono-exfoliation mechanism of graphite. It was revealed that shock waves with a pressure magnitude of up to 5 MPa and liquid-jets with velocities of ca. 80 ms^{-1} from transient cavitation bubble implosions were essential for the initiation and propagation of the exfoliation process. On the other hand, bubble oscillations associated with stable cavitation were beneficial for promoting gentler delamination of graphite layers.[53]

3.2 | Structural analysis

The XRD patterns of ACHS (1:3, 900, 2) and Exf. ACHS (1:3, 900, 2) samples are shown in Figure 2A and the XRD patterns of the remaining samples prepared under different experimental conditions are shown in Figure S1B (Supporting information). The appearance of broad peak at $2\theta = 26°$ and weak intensity peak at $2\theta = 43°$ correspond to the (002) and (100) planes of
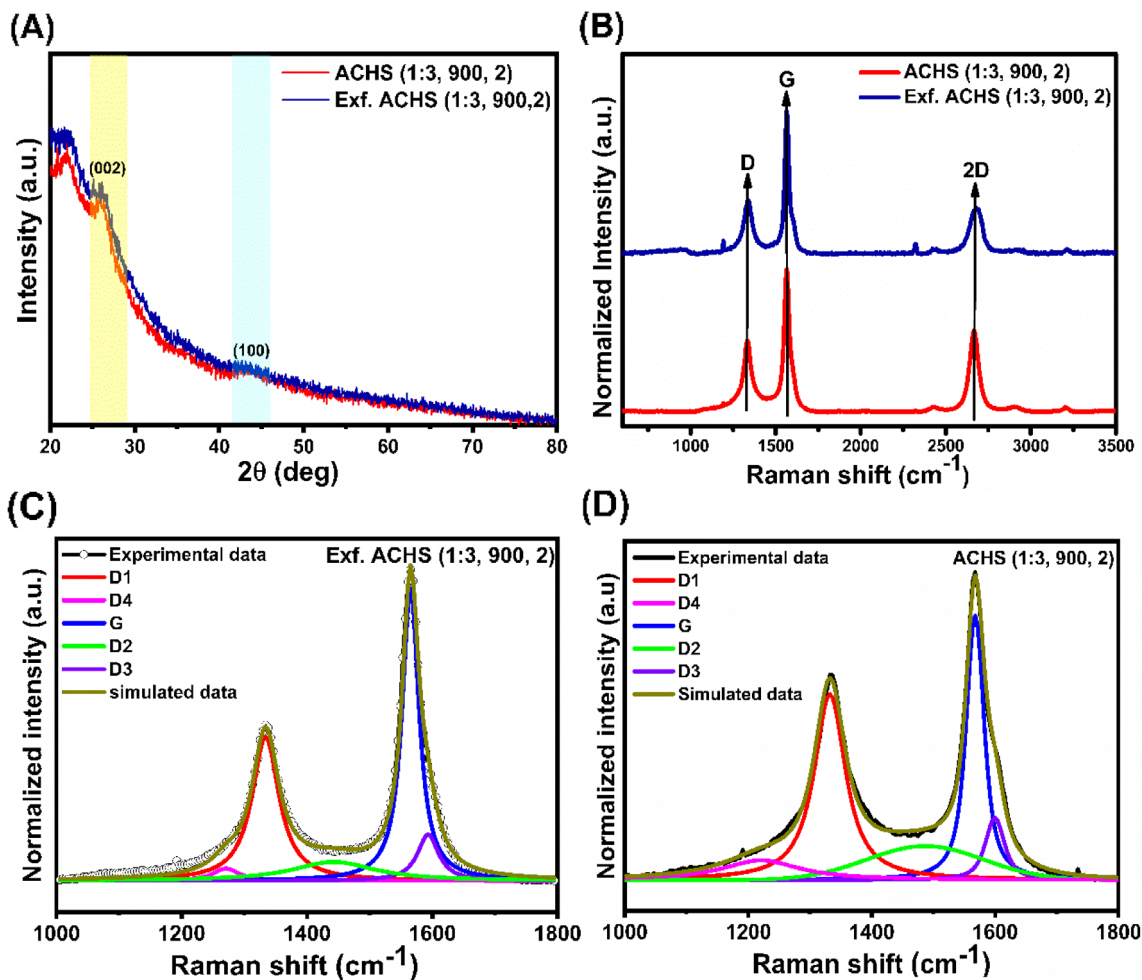
FIGURE 2   (A) XRD patterns of ACHS (1:3, 900, 2) and Exf. ACHS (1:3, 900, 2) samples (B) Raman spectra of activated carbon samples Exf. ACHS (1:3, 900, 2) and ACHS (1:3, 900, 2) (C) Deconvoluted Raman spectra of Exf. ACHS (1:3, 900, 2) (D) Deconvoluted Raman spectra of ACHS (1:3, 900, 2)

graphitic carbon respectively.[54,55] The existence of a broad peak at $2\theta = 23°$ in all of the samples is due to the background intensity developed by the amorphous and disordered carbon structures.[56] The Raman spectra of Exf.ACHS (1:3, 900, 2) and ACHS (1:3, 900, 2) samples are shown in Figure 2B and those for the rest of chemically activated ACHS samples, sono-exfoliated ACHS samples are shown in Figure S1C,D, respectively (Supporting information). All the spectra consist of two prominent peaks at 1336 and 1567 cm^{-1} which are ascribed to the D and G bands respectively.[39,57] The D-band corresponds to the in-plane vibrations of disordered sp^2 carbon atoms whereas the G-band arises from the in-plane vibrations of sp^2 bonded graphitic carbon structures.[57] The D and G bands of these biomass derived activated carbon samples are shifted to lower wavenumbers when compared to traditional graphene[58] (D band: ~1350 cm^{-1} and G band: ~1590 cm^{-1}) which may be due to external factors such as differences in the

preparation conditions, mechanical compression and thermal expansion etc.[59] The position of the G-band is particularly sensitive to the number of layers present in a graphene sample. As the number of layers increases, the band shifts to a lower wave number representing a slight softening of the bonds with each addition of a graphene layer.[60,61] The sono-exfoliation process used in this work resulted in delamination creating a greater number of graphene-like layers in the exfoliated sample, as shown in the HRTEM in Figure 3B. The presence of multiple layers in the carbon framework shifted the position of G-band to lower wave number than that of traditional single or bi-layer graphene.[52] The Raman peaks corresponding to D and G bands are further deconvoluted into five peaks.[62] The fitting method employed was Voigt fitting as shown in Figure 2C,D and the corresponding parameters employed for peak fitting are given in Supplementary Information Table S1 for both Exf. ACHS (1:3, 900, 2) and ACHS (1:3, 900, 2) samples. The spectra of both
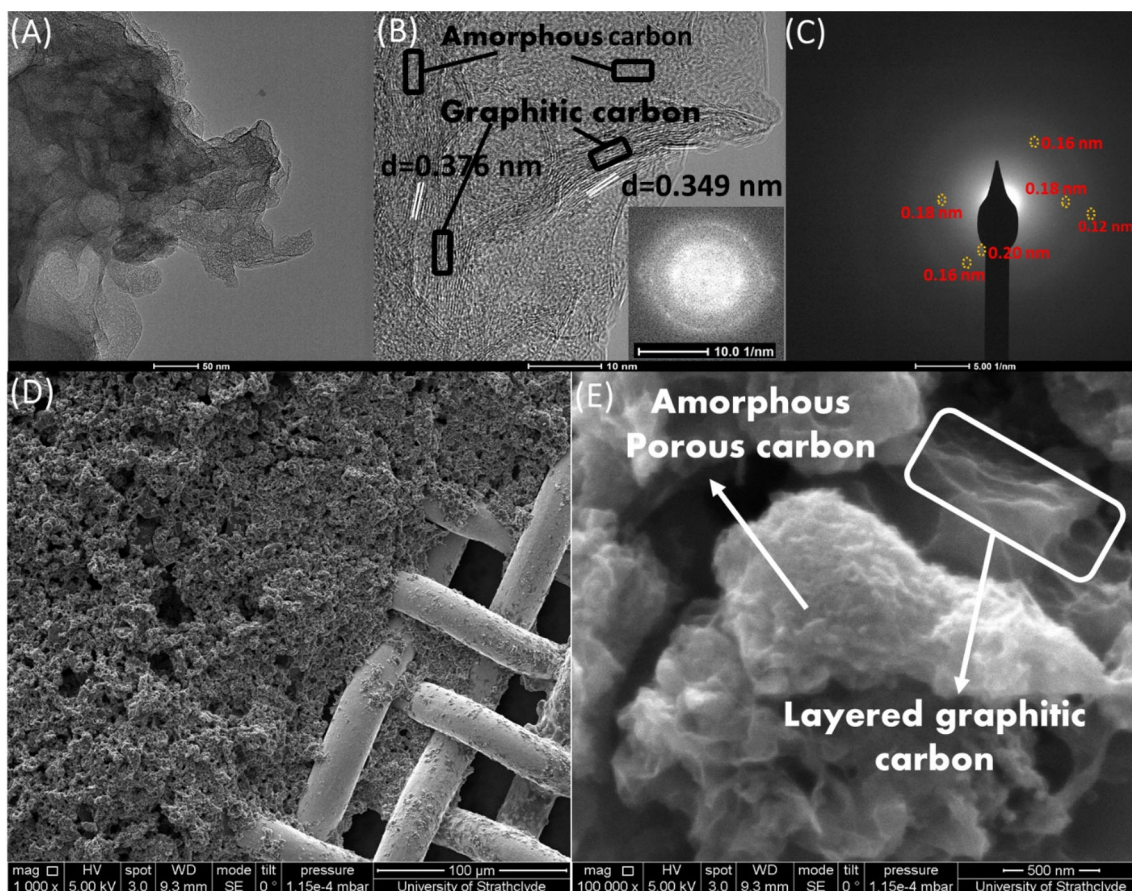
FIGURE 3 (A-B) Transmission electroscope microscope (TEM) and High-Resolution TEM images of Exf. ACHS (1:3, 900, 2) sample at different magnifications with FFT image of corresponding graphic layers in the inset (C) Selected area diffraction pattern of Exf. ACHS (1:3, 900, 2) sample (D) Field Emission Scanning Electron Microscopy image of Exf. ACHS (1:3, 900, 2) sample coated on stainless steel mesh electrode (E) Magnified images of Exf. ACHS (1:3, 900, 2) coated on stainless steel mesh electrode

samples include: D1-band at 1336 ± 1 cm^{-1}, G-band at 1567 ± 1 cm^{-1}, D3-band at 1600 cm^{-1}, D2-band at 1453 ± 20 cm^{-1}, and D4 band at 1270 cm^{-1}.[62] The small peak at 1270 cm^{-1} is ascribed to the disordered graphitic lattice. The D1-band arises as a consequence of lattice disturbance/defects present in the carbon materials. In general, Raman spectra of pure and high-quality graphene do not show the D-band. However, in the case of activated carbon, the D-band always appears in the Raman spectrum, indicating disorder of the carbonaceous layers. The broad D-band is a result of the heterogeneity and the presence of amorphous carbon or graphite. The D2 band corresponds to the amorphous carbon material present along with the distorted graphitic lattice of carbonaceous material. The D3 band in the spectra is related to lattice vibration that corresponds to the G peak in the bulk of a carbon material.[59,63] The degree of graphitization of all the samples is assessed using the ratio of area under the D and G bands (I_{D1}/I_G). The lower the I_{D1}/I_G ratio, the higher the degree of graphitization. The I_{D1}/I_G values calculated from the area under the D1 and G

bands are given in Table S1. The I_{D1}/I_G ratio of the chemically activated ACHS (1:3, 900, 2) sample is the lowest (0.98) of all the chemically activated samples indicating that a high degree of graphitization can be achieved for the sample activated with carbon: KHCO$_3$ ratio of 1:3, at temperature of 900°C and holding time of 2 h. The degree of graphitization is further increased during the sono-exfoliation process thus separating the graphitic layers leading to a decrease in the I_{D1}/I_G ratio (0.78). The lower I_{D1}/I_G values suggest that the mechanically exfoliated sample has a lower number of disordered carbon structures and more aromatic ring structures compared to other chemically activated samples.[13]

In order to get the information related to the molecular structure (especially functional groups and bonds) of the carbon material before and after exfoliation, Fourier transform-infrared (FTIR) spectra of the samples were collected and compared with each other as shown in Figure S1E (Supporting information). FTIR spectra of hazelnut shell derived activated carbon before exfoliation [ACHS (1:3, 900, 2)] and after exfoliation [Exf. ACHS

(1:3, 900, 2)] are shown in Figure S1E. The spectra consists of a broad peak between 1000 and 1300 cm^{-1} corresponding to stretching vibration in C-O-C bonds. Two characteristic peaks at 1574 and 1427 cm^{-1} are ascribed to the C $=$ C stretching vibration in aromatic carbon rings and C-H stretching vibration respectively.[64,65] The broad peak at 3400 cm^{-1} is attributed the O-H stretching vibration in carbonyl and phenyl groups.[65] It can be observed from the spectra that the intensity of C $=$ C band increased after sono-exfoliation process indicating that this process can overcome the van der Waals forces between the activated carbons and increase the C $=$ C bond content in the overall sample.

3.3 │ Morphological analysis

TEM images of chemically activated ACHS (1:3, 900, 2) sample and sono-exfoliated Exf. ACHS (1:3, 900, 2) sample are shown, respectively, in Figure S2A,B and in Figure 3A,B. The TEM images of Exf. ACHS (1:3, 900, 2) and ACHS (1:3, 900, 2) clearly indicates the presence of ultrathin graphitized layers accumulated in the porous carbon framework. TEM analysis revealed that the ACHS (1:3, 900, 2) have few regions of graphitic carbon layers in comparison to Exf. ACHS (1:3, 900, 2) sample which consists of multilayers that are clearly observed in the high resolution TEM (HRTEM) images shown in Figure 3B. The porous nature was caused by the corrosion of KHCO$_3$ under a high temperature of 900°C, whereas the sono-exfoliation further delaminates the microstructure of the activated carbon resulting in the formation of multi-layered graphene-like carbon nanosheets. Moreover, the spacing between the graphitic layers has been increased (as seen from Figure 3B) after sono-exfoliation which improves ion-transport properties inside the porous framework and restricts the stacking of these graphitic layers during the continuous cycling process. Porous activated frameworks with graphene-like features are particularly beneficial for supercapacitor applications because the amorphous carbon provides interconnected channels for the movement of electrolyte ions inside the pores whereas the graphitic carbon promotes fast ion-diffusion kinetics and charge storage at the electrode/electrolyte interface. The Fast Fourier transform (FFT) image of exfoliated graphene like carbon with multi-layers are shown in the inset of Figure 3B, which displays ring pattern formed from closely spaced diffraction spots corresponding to hexagonal sp^2 carbon structures of the multilayer graphene.[66] The selected area diffraction pattern (SAED) showed the presence of amorphous phase indicating the porous nature of the sample whereas the presence of faint diffraction spots along the

rings reveals crystallinity in the lattice structure due to the presence of graphitic carbon enclosed in the porous carbon framework.

The morphology of the Exf. ACHS (1:3, 900, 2) sample coated on stainless steel mesh electrodes was viewed using FESEM (shown in Figure 3D). The structure of the sono-exfoliated sample is composed of agglomerated multilayer graphene-like carbon nanosheets with porous amorphous carbon. The magnified image shown in Figure 3E clearly shows the heterogeneity of the sono-exfoliated sample consisting of porous amorphous carbon and layered graphitic carbon.

3.4 │ Compositional analysis

The chemical characteristics of Exf. ACHS (1:3, 900, 2) and ACHS (1:3, 900, 2) was further analysed using XPS. The survey scan of Exf. ACHS (1:3, 900, 2) is shown in Figure 4A and the ACHS (1:3, 900, 2) sample is shown in Figure S3A (Supporting information). The XPS spectra of the as-prepared samples reveals the presence of oxygen and nitrogen in addition to carbon, with O1s, N1s and C1s peaks at 532 eV, 400 eV, and 284.5 eV respectively. In order to analyse the nature of the heteroatoms present in the as-prepared activated carbon samples, peak deconvolution was performed and the corresponding parameters are shown in Tables S2 and S3. The C1s spectra of the samples are shown in Figure 4B and Figure S3B (Supporting information). The C1s peaks have been deconvoluted into four peaks centered at 284.5 eV (C-C/ C $=$ C), 285.3 eV (C-O), 286.39 eV (C $=$ O), and 288 $\pm$ 0.2 eV (C-N)[67-70] whereas the Exf. ACHS (1:3, 900, 2) sample consists of one extra peak at 283.3 eV corresponding to the C-C bond[71] which can occur after sono-exfoliation process. The 284.5 peak in the C1s spectrum of the samples reveals that both the products (before and after exfoliation) have graphite-like sp^2 hybrid carbon. In addition, the area under the peak at 284.5 eV is larger in Exf. ACHS (1:3, 900, 2) than ACHS (1:3, 900, 2), which indicates the content of sp^2 is greater in the sono-exfoliated graphene-like activated carbon. XPS results of C1s spectra are in good agreement with the Raman results where the I_{D1}/I_G ratio in the sono-exfoliated sample is lower, indicating sono-exfoliation improved the quantity of sp^2 hybridized graphitic carbons. Also, the presence of O, N-based functional groups on the carbon framework has been shown to enhance the wettability and provide additional sites for charge storage.[67] The deconvoluted O1s spectra of Exf. ACHS (1:3, 900, 2) confirms the presence of C $=$ O, C-O, and carboxyl functional groups at the binding energy of 531.2, 532.5, and 534.2 eV respectively (Figure 4C).[71,72] The trace amount
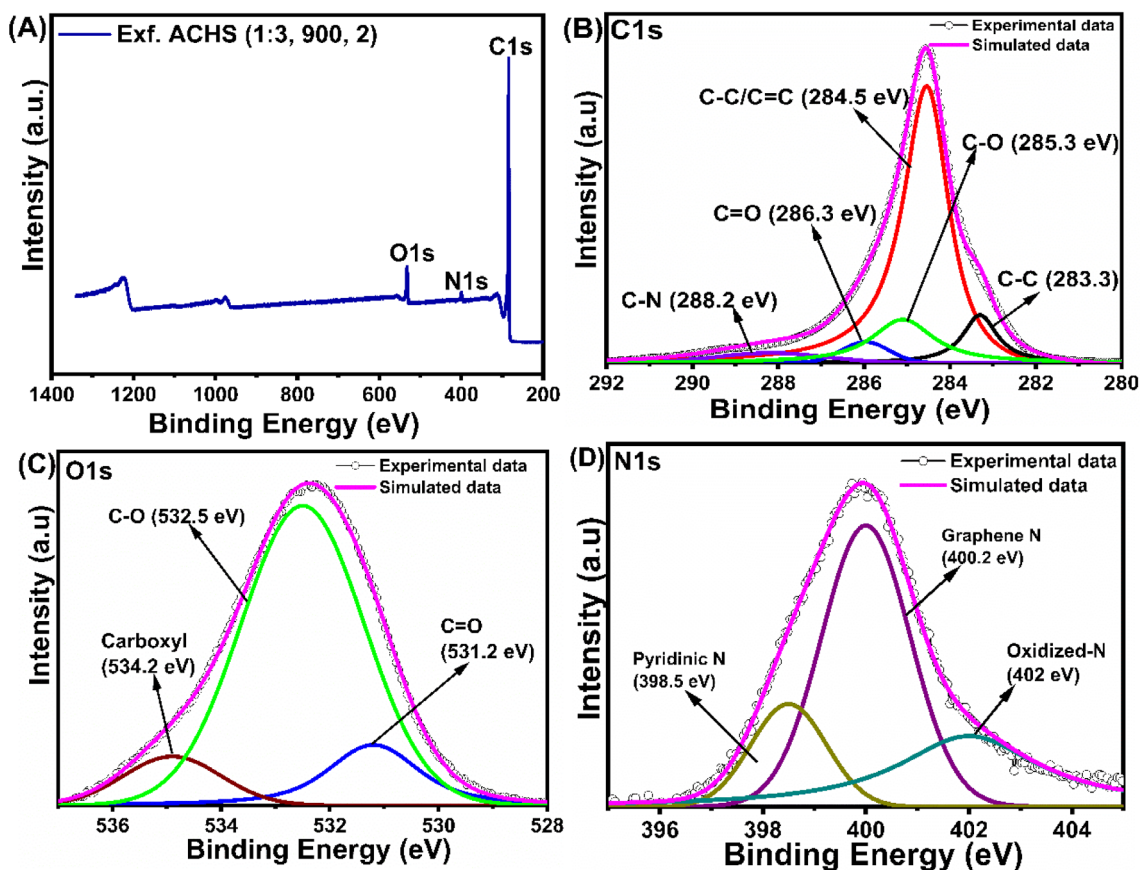
FIGURE 4   (A) XPS survey spectra and high resolution (B) C1s (C) O1s and (D) N1s core level spectra of Exf. ACHS (1:3, 900, 2)

of nitrogen functionalities in the as-prepared sample are further characterized by deconvoluting N1s spectra. The N1s spectra of Exf. ACHS (1:3, 900, 2) is shown in Figure 4D and consists of three types of N bonded in the form of pyridine-N, graphene-N, and oxidized-N positioned at 398.5 eV, 400.2 eV, and 402 eV whereas ACHS (1:3, 900, 2), shown in Figure S3D, is composed of trace amounts of only graphene-N and pyridine-N.[73,74] The area under the graphene-N peak is greater in sono-exfoliated sample Exf. ACHS (1:3, 900, 2) than in the chemically activated sample ACHS (1:3, 900,2). This additional graphene-N content might be linked to the increase in surface area where graphene-N becomes active after the sono-exfoliation process. Sono-exfoliation resulted in further etching of the carbon framework creating more pores at nitrogen atom locations in the carbon framework. The elemental composition (ie, the relative concentration of C, N, and O present in the samples) was calculated from the core energy levels of individual elements using peak intensities. Before considering the peak intensities, the core energy levels were normalized to number of sweeps. Exf. ACHS (1:3, 900, 2) was primarily composed of 91.97% C, 1.2% N, and 6.83% O with heteroatoms (N, O) originating from the hazelnut shells itself.

On the other hand, the ACHS (1:3, 900, 2) sample consisted of 87.69% C, 0.51% N, and 11.8% O respectively. As previously stated, the increase in N content might be linked to the sono-exfoliation procedure which led to further etching of the carbon framework, resulting in the formation of new pores. Moreover, the increase in C content after exfoliation indicates that high quality sp^2 carbon materials can be obtained by simple exfoliation of chemically activated carbon. From the XPS analysis, it was confirmed that the prepared samples mainly consisted of oxygen functional groups with trace amounts of nitrogen functionalities on the carbon framework. It is generally observed that activated carbon with O, N- heteroatoms play a positive role in providing additional pseudocapacitance, hydrophilicity, and promotes electron transfer rate of the electrode material.[67,75,76]

3.5 | Effect of sono-exfoliation on structural and morphological characteristics of activated carbon

In this work, sono-exfoliation was employed to improve the specific surface area and degree of graphitization of

activated carbon. Ultrasonic waves produce various distinct properties in liquids by acoustic cavitation, such as bubble formation, growth, and implosive bubble collapse as shown in Figure 5A, which can be used to exfoliate the graphitic carbon trapped within the porous carbon. According to the literature, during acoustic cavitation, extreme pressures and temperatures are created, triggering a variety of physical and chemical reactions inside the solution.[77,78] When a bubble begins to explode, high-pressure shock waves spread across the liquid media at enormous velocities which are expected to exfoliate/separate the graphitic carbon layers that are trapped inside the bulk amorphous carbons as shown in Figure 5B,C. As a result, the van der Waals interactions between agglomerated carbon particles are broken, resulting in an increase in $C = C$ content in activated carbons. The increase in $C = C$ is clearly visible in C1s XPS spectra of Exf. ACHS (1:3, 900, 2) as compared to ACHS (1:3, 900, 2) shown in Figure 4B and Figure S3B where the area under $C = C$ peak (284.5 eV) increased after sono-exfoliation process. The decrease in I_{D1}/I_G also shows the significance of sono-exfoliation in increasing the graphitic content in the exfoliated Exf. ACHS (1:3900, 2) sample. Moreover, use of sulfuric acid (H_2SO_4) in the sonication process further corrodes the surface of the porous carbon framework resulting in the increase in specific surface area and pore volume as shown in Table 1. The effect of sono-exfoliation can also be found in high resolution TEM images shown in Figure 3B and Figure S2B where the number of graphitic layers found in Exf. ACHS (1:3, 900, 2) (Figure 3B) are more compared to ACHS (1:3, 900, 2) (Figure S3B) and the spacing between the layers is larger in the former as compared to

latter. This indicates that the graphitic carbon layers that are accumulated inside the chemically activated carbon are loosened further because of the breaking of van der Waals interactions between the agglomeration carbon particles due to sono-exfoliation process. Furthermore, after sono-exfoliation, the space between the graphitic layers has been enhanced, which improves ion-transport characteristics inside the porous framework and prevents the graphitic layers from stacking during the continuous cycling process. According to the results of this study, sono-exfoliation of biomass activated carbon appears to be a potential method for producing high surface area graphene like activated carbon materials with potentially good electrochemical performance.

3.6 | Electrochemical energy storage analysis

The electrical conductivity of Exf. ACHS (1:3, 900, 2) and ACHS (1:3, 900, 2) powder samples was conducted to check the material's ability to conduct electrical current. These measurements are performed using two probe method using Linear Sweep Voltammetry (LSV) technique. Figure S4B (Supporting information) shows the I-V graph of pellets made using Exf. ACHS (1:3, 900, 2) and ACHS (1:3, 900, 2) measured at 5 mV s^{-1} scan rate using LSV technique. The slope of the I-V graph in Figure S4B was then substituted in Equation (1) to obtain the electrical conductivity of the powder samples. The conductivity of Exf. ACHS (1:3, 900, 2) was found to be 1.53×10^2 S/m whereas that of ACHS (1:3, 900, 2) was calculated as 0.49×10^2 S/m. The high SSA and
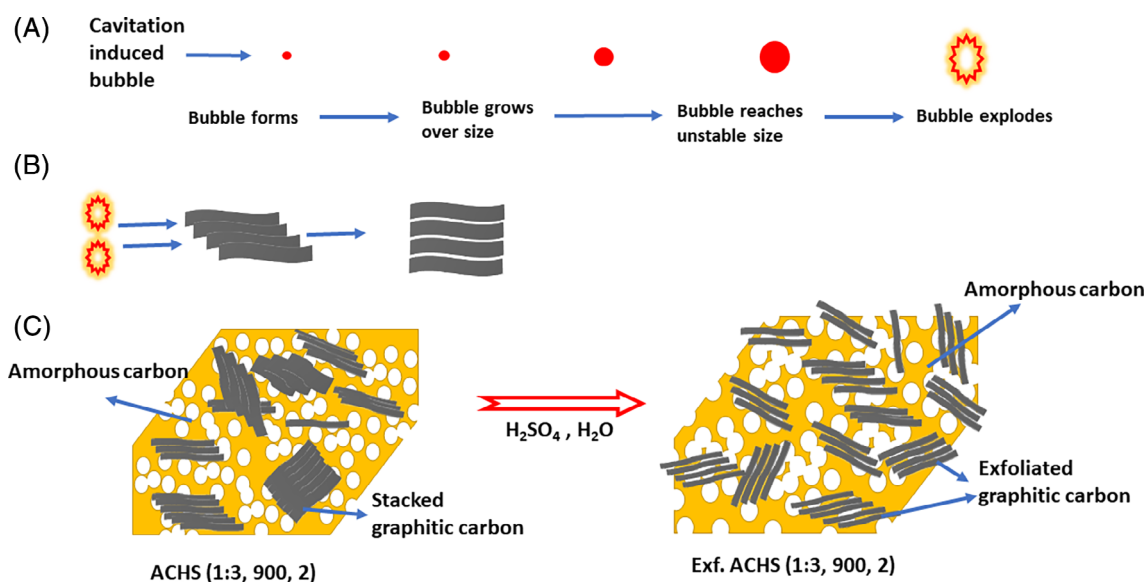

FIGURE 5 Illustration of possible mechanism of porous activated carbon exfoliation

improved degree of graphitization resulted in enhanced electrical conductivity and reduced electrical resistance for sono-exfoliated Exf. ACHS (1:3, 900, 2) sample as compared to chemically activated ACHS (1:3, 900, 2) sample. After performing electrical conductivity measurements, the energy storage performance of the as-synthesized ACHS samples coated on stainless steel electrodes were investigated employing 1.0 M Na_2SO_4 aqueous electrolyte in a three-electrode configuration. Figure 6A and Figure S5A,D (Supporting information) shows the CV curves of the as-synthesized samples. The cyclic voltammogram of all samples demonstrated rectangular shaped curves within the −0.1 to 0.9 V operating potential window (measured at a scan rate of 5 mV s^{-1}), which is a characteristic behavior of porous carbonaceous materials. From Figure 6A it can be deduced that the Exf. ACHS (1:3, 900, 2) sample exhibited a higher current and a larger loop area indicating that a greater number of active pores are participating in the charge storage mechanism.[79] The reason behind this exceptional performance is that the Exf. ACHS (1:3, 900, 2) sample possesses a much higher specific surface area and pore volume compared to all other samples (Table 2), due to greater degree of graphitization, which is evident from the lower I_{D1}/I_G values and higher N content. The presence of electron donor heteroatoms such as N serves as an electron lone pair to the amorphous carbon framework to enhance the electron conductivity and provide pseudocapacitance.[80] Furthermore, N-doping improves the wettability of the electrode materials making it easier for the electrolyte ions to reach the internal pores of the carbon framework. The wettability of the electrode surface to the electrolyte was verified using the contact angle measurement which is used to study the interaction between the electrode surface and probing liquid.[81] In the present work, contact angle measurements were performed on Exf. ACHS (1:3, 900, 2) and ACHS (1:3, 900, 2) coated mesh electrodes employing stationary water contact angle using 1 M Na_2SO_4 aqueous electrolyte as the probing solvent as shown in Figure 6E,F. The electrolyte contact angle of Exf. ACHS (1:3, 900, 2) electrode has been drastically reduced to 86.5^0 (as shown in Figure 6E) as compared to 100^0 of ACHS (1:3, 900, 2) electrode indicating better wettability of sono-exfoliated sample. After sono-exfoliation, the electrolyte contact angle has been much improved which can be ascribed to the improved N-content of the sono-exfoliated sample. The process of sono-exfoliation improved the surface area and pore volume resulting in a larger number of micro/meso pores in the activated carbon framework thereby providing more accessibility to the electrolyte ions and improving the ionic transport. The CV curves of the Exf. ACHS (1:3, 900, 2) sample are shown in Figure 6B and resemble a quasi-rectangular

shape at higher scan rates within the operating potential window range, indicating the superior capacitive behavior at higher scan rates. The reason for this quasi-rectangular behavior is the insufficient reaction time for the electrolyte ions to access/pass through the deeper pores of the electrode, resulting in the distortion of its double layer behaviour.[82] More specifically, the electrolyte ions diffuse through the inner pores of the electrode material at lower scan rates where the entire active surface sites of the electrode material might be utilized during the adsorption/desorption process. In contrast, the ionic movement in the electrolyte is restricted at higher scan rates due to the limited reaction time and so, only the external surface area of the material is utilized for charge storage.[83]

Figure 6C and Figure S5B,E (Supporting information) shows the Nyquist plots of all of the ACHS samples. It can be observed from Figure 6C that the Exf. ACHS (1:3, 900, 2) sample shows a nearly straight line in the low frequency region and a semicircle in high frequency region indicating ideal capacitor behaviour.[84] The x-intercept in the high frequency region represents the equivalent series resistance (R_s) which is a combination of the resistance of the electrolyte, internal resistance of the active materials and the substrate, and the contact resistance with the collector.[85] The equivalent series resistance of the ACHS (1:3, 900, 2) and Exf. ACHS (1:3, 900, 2) sample were found to be ~4.82 and 2.71 Ω respectively. In the medium frequency region, the projected length of the Warburg-type line on the real axis represents the ion diffusion process from the electrolyte into the electrode materials.[86] The exfoliated sample showed the shortest projected line on the real axis, implying superior ion diffusion. Furthermore, the small semicircle in the middle frequency region correspond to the electron transfer process. It can be seen that the exfoliated sample has the smallest semicircle diameter among all the samples, indicating the lowest charge transfer resistance (R_{ct}) of 0.69 Ω with most efficient charge transfer process. Figure 6D shows the Bode plot of the exfoliated ACHS sample. A phase angle of 75.48° at low frequencies was observed for Exf. ACHS (1:3, 900, 2) which is nearly equal to an ideal capacitive (C) behavior whereas the phase angle of ACHS (1:3, 900, 2) was found to be 64.97°. In addition, the characteristic frequency f_o for the phase angle of 45° is 0.19 Hz, which corresponds to a relaxation time constant ($\tau_0 = 1/f_0$) of 5.26 secs. The characteristic frequency and relaxation time of chemically activated carbon sample before exfoliation [ACHS (1:3, 900, 2)] was found to be 0.08 Hz and 12.5 s which are considerably higher than for the sono-exfoliated sample. The relaxation time for a supercapacitor simply means that the energy stored within a supercapacitor can be released
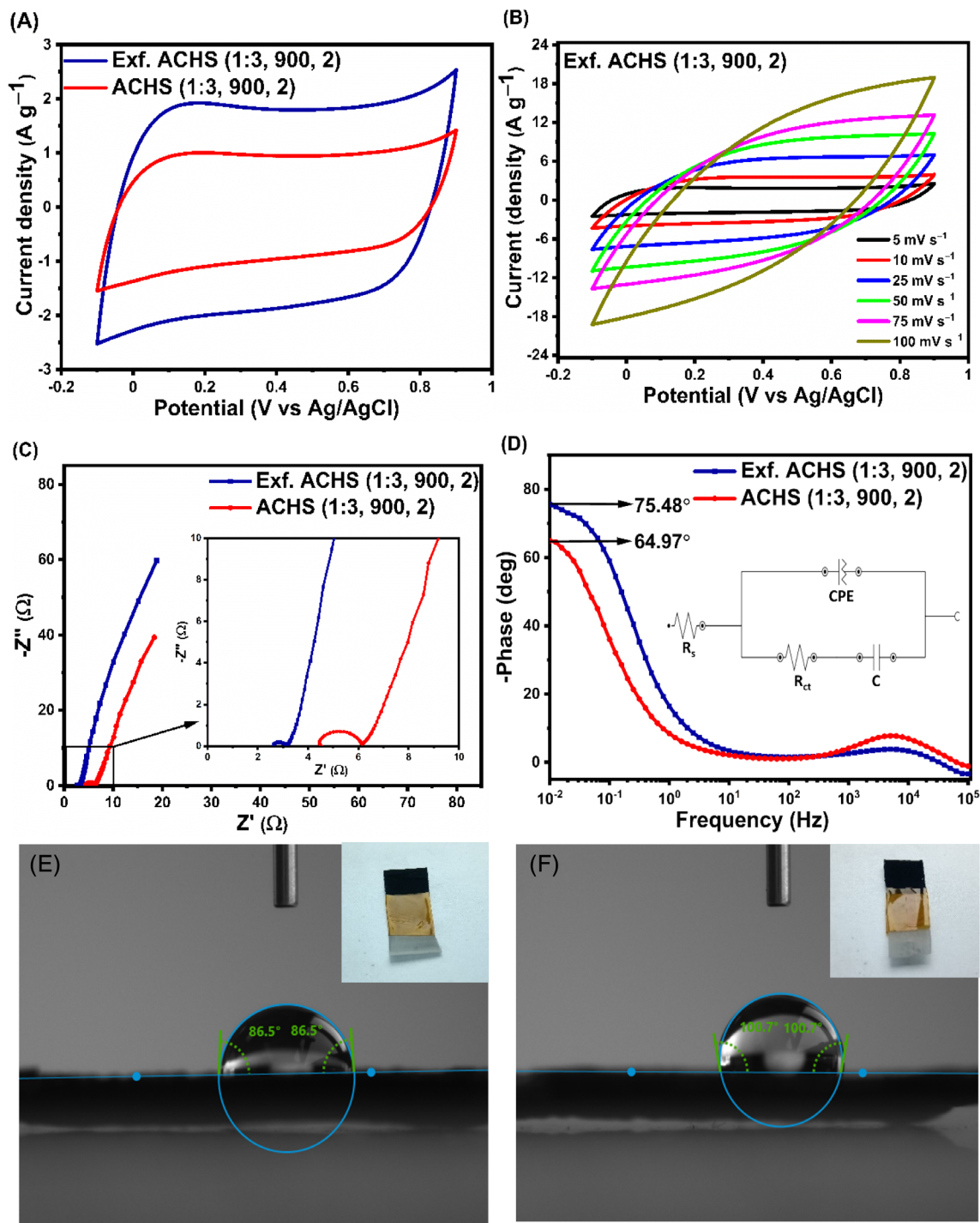
FIGURE 6   (A) Cyclic Voltammetry (CV) at 5 mV s^{-1} scan rate of ACHS (1:3, 900, 2) sample before and after exfoliation (B) CV of Exf. ACHS (1:3, 900, 2) at different scan rates from 5-100 mV s^{-1} (C) Nyquist plot for ACHS (1:3, 900, 2) sample before and after exfoliation. Inset shows the magnified Nyquist plots (D) Phase plot ACHS (1:3, 900, 2) sample before and after exfoliation. Inset shows the equivalent circuit used to fit the Nyquist plots. All these measurements were carried out in 1 M Na$_2$SO$_4$ aqueous electrolyte in 3-electrode configuration (E) Contact angle of Exf. ACHS (1:3, 900, 2) electrode (F) Contact angle of ACHS (1:3, 900, 2) electrode with inset showing the mesh electrodes used for electrochemical and contact angle testing

within a period of 5.26 s at 0.21 Hz frequency.[87] The inset of Figure 6D shows the equivalent circuit utilized for fitting the Nyquist plot for the Exf. ACHS (1:3, 900, 2) sample. The equivalent circuit is fitted with four different

components: R$_s$ corresponds to the equivalent series resistance, R$_{ct}$ corresponds to the charge transfer resistance, CPE corresponds to the constant phase element, and C corresponds to the Capacitive element respectively.

At high frequencies, the R_{ct}-CPE circuit is responsible for the transfer of ions between the micro/mesopores of the electrode material, whereas the nearly straight line at low frequency region is indicative of ideal capacitive behavior which is in accordance with Nyquist plots. The capacitive behavior is indicated by the **C** element in the equivalent circuit

Figure 7A and Figure S5C,F (Supporting information) shows the GCD curves of the as-prepared samples at 0.5 A g^{-1} current density. The GCD curves of all samples displayed quasi-linear charge discharge characteristic indicating the double layer behavior of all the carbonaceous samples. Moreover, the GCD curve of mechanically exfoliated Exf. ACHS (1:3, 900, 2) electrode at 0.5 A g^{-1} current density showed a symmetric charge/discharge curve with longer charge discharge duration indicating a larger number of electrolyte ions have participated in the charge/discharge process. The higher N content and specific surface area of the Exf. ACHS (1:3, 900, 2) sample provided more accessible sites for the electrolyte ions making the sono-exfoliated sample an excellent electrode material for supercapacitor applications than the chemically activated samples. Figure 7B demonstrates the rate capability of the device at higher current densities. The electrode material maintained its quasi-linear charge/discharge nature indicating the stability of the electrode at higher current densities. The specific capacitance of the Exf. ACHS (1:3, 900, 2) sample was calculated using Equation (2) (experimental section) and found to be 320.9 F g^{-1} at 0.2 A g^{-1} current density and it reduced to 150 F g^{-1} at a high current density of 30 A g^{-1}, clearly demonstrating the rate capability of the exfoliated sample, where 46.7% of its capacitance is retained at higher current densities. This reduction in C_s with increasing current density can be understood since at higher current densities the electrolyte ions have minimum probability to access the inner pores of the electrode material. This significantly reduces the electro-active surface area

hindering the formation of a double layer and decreasing the value of C_s at higher current densities[88]

In Table 3, the specific surface area and specific capacitance of our carbon electrodes is compared with the carbonaceous electrodes obtained from different plant based, fruit based, and nutshells-based waste biomass precursors reported in recently in the literature. The morphologies of the most reported carbonaceous materials from hazelnut shells,[93] palm shells,[12] and coconut-shells[10] was found to be dominated by a porous nature with specific capacitance in the range of 170–350 F g^{-1}. On the contrary, micro/nano-porous carbons from peanut shells,[13] coconut shells[91] possess dual morphology, with porous carbons and sheet like morphology, but their specific capacitance is limited to 186–268 F g^{-1} due to a lower specific surface area. Hence, in order to increase the specific capacitance, it is necessary to synthesize carbon materials with high layered structure and well-distributed pore network without compromising its specific surface area and pore network in a simple and economic way. From the results presented in this study, it can be observed that the sono-exfoliated Exf. ACHS (1:3, 900, 2) graphene-like activated carbon electrodes possess all the above-mentioned qualities with the specific capacitance 1.71 times higher than similar graphene-like morphologies derived from waste peanut shells (186 F g^{-1}).[13] Table 3 further reveals that the sono-exfoliated sample obtained from the hazelnut shells in the present study has comparable, or higher, specific capacitance than the activated carbon from hazelnut shells with substantially larger specific surface area reported in literature. For example, Xie et al.[93] reported the preparation of high surface area porous activated carbon from hazelnut shells using two activating agents, zinc nitrate [$Zn(NO_3)_2$], and potassium hydroxide (KOH), with a specific capacitance of 239.8 F g^{-1} which is lower than that of Exf. ACHS (1:3, 900, 2) reported in the present work [280.2 F g^{-1} at 0.5 A g^{-1}]. Similarly, Liu et al.[94] reported the preparation

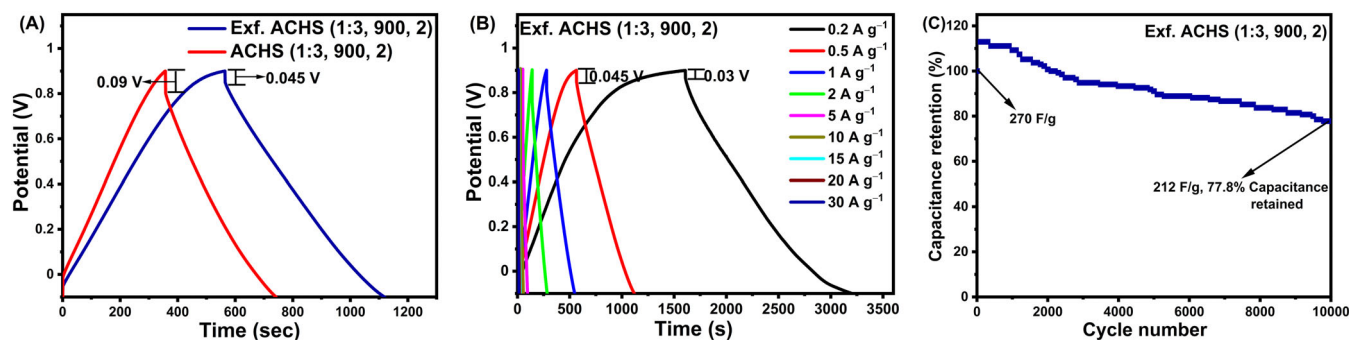**FIGURE 7** (A) Galvanostatic charge-discharge (GCD) at 0.5 A g^{-1} current density of ACHS (1:3, 900, 2) sample before and after exfoliation (B) GCD of Exf. ACHS (1:3, 900, 2) at different current densities (C) Cyclic stability profile of Exf. ACHS (1:3, 900, 2) coated stainless steel electrode over 10 000 cycles at 2 A g^{-1} current density in 1 M Na_2SO_4 aqueous electrolyte using 3-electrode configuration

TABLE 3 Comparison of specific surface area (SSA) and specific capacitance (Cs) values for various nut-shells derived activated carbon produced under different experimental conditions recently reported in literature

Biomass	SSA ($m^2 g^{-1}$)	Specific Capacitance (C_s)	Electrolyte	References
Chestnut shells	1252.5	173 $F g^{-1}$ at 0.1 $A g^{-1}$	6 M KOH	[89]
Chestnut shells	1829.7	238.2 $F g^{-1}$ at 0.1 $A g^{-1}$	6 M KOH	[90]
Coconut shells	1559	228 $F g^{-1}$ at 5 $mV s^{-1}$	6 M KOH	[91]
Coconut shells	1874	268 $F g^{-1}$ at 1 $A g^{-1}$	6 M KOH	[92]
Palm shells		74.76 $F g^{-1}$ at 0.3 $A g^{-1}$	1 M H_2SO_4	[12]
Peanut shells	2070	186 $F g^{-1}$ at 0.5 $A g^{-1}$	1 M H_2SO_4	[13]
Hazelnut shells	2694	239.8 $F g^{-1}$ at 0.5 $A g^{-1}$	6 M KOH	[93]
Hazelnut shells	3469	338 $F g^{-1}$ at 0.2 $A g^{-1}$	1 M Na_2SO_4	[94]
Grape marcs	2221.4	310 $F g^{-1}$ at 0.5 $A g^{-1}$	1 M Na_2SO_4	[95]
Cashew nut shells	900	214 $F g^{-1}$ at 1 $A g^{-1}$	1 M Na_2SO_4	[96]
Macadamia nut shells	2806	155 $F g^{-1}$ at 1 $A g^{-1}$	1 M Na_2SO_4	[97]
Pineapple leaves		131.5 $F g^{-1}$ at 5 $mV s^{-1}$	1 M Na_2SO_4	[98]
Coffee grounds	1960.1	287.9 $F g^{-1}$ at 2 $mV s^{-1}$	1 M Na_2SO_4	[99]
Areca fibers	250	47 $F g^{-1}$	0.1 M Na_2SO_4	[100]
Banana fibers	1097	74 $F g^{-1}$ at 0.02 $A g^{-1}$	1 M Na_2SO_4	[101]
Peanut shells	1481.59	239.88 $F g^{-1}$ at 0.5 $A g^{-1}$	1 M Na_2SO_4	[102]
Hazelnut shells	2545	320.9 $F g^{-1}$ at 0.2 $A g^{-1}$	1 M Na_2SO_4	This work

of activated carbon from hazelnut shells via KOH and phosphoric acid (H_3PO_4) activation which have a 26.6% higher specific surface area than the current study but the C_s are of the same order of magnitude, mainly due to the P-doping caused by H_3PO_4 activation. Furthermore, as shown in Table 3, the sono-exfoliated activated carbon obtained from hazelnut shells showed higher electro-chemical performance compared to the activated carbon obtained from cashew nut shells,[96] macadamia nut shells,[97] pineapple leaves,[98] coffee grounds,[99] banana fibers,[101] grape marcs,[95] and peanut shells[102] tested using 1 M Na_2SO_4 as electrolyte. From these examples, it can be concluded that the sono-exfoliation, rather than utilizing additional high temperature chemical activation, is an excellent room temperature approach to enhance the electrochemical performance of activated carbon samples. The high specific capacitance of Exf. ACHS (1:3, 900, 2) can be attributed to the high specific surface area and pore volume which provided more/wide active sites for the electrolyte ions to access the carbon framework whereas the graphene-like morphology offered low resistance pathways within the interconnected carbon framework for easier ionic diffusion during the charging/discharging process. The energy and power density of the electrode material are calculated using Equation (3) and (4). The Exf. ACHS (1:3, 900, 2) electrode material exhibited maximal energy density of 44.56 Wh kg^{-1} at a power density of 102.11 W kg^{-1} at 0.2 A g^{-1} and it retained

~46.7% of its energy density even under a high-power output of 14 976 W kg^{-1}, which clearly demonstrates that the mechanically exfoliated sample has superior ability to deliver stable energy while encountering high power. The mechanical exfoliation of chemically activated carbon not only facilitated the high surface area and pore volume combined with layered morphology, but also provided more/wide active sites for the electrolyte ions to access the carbon framework.

The electrochemical cyclic retention of the Exf. ACHS (1:3, 900, 2) supercapacitor electrode was investigated under constant current charge/discharge method. Figure 7C shows the percentage cyclic stability of the electrode examined for 10 000 cycles at 2 A g^{-1} current density ran over 19 days continuously without changing the electrolyte during these cycles. It can be observed that the percentage retention of capacitance increases for the first 2100 cycles from 100% to 112.9%. This increase in percentage capacitance retention may be due to the complete activation of porous carbon electrode framework for the adsorption/desorption of the electrolyte ions during the initial 2100 cycles. Hence the capacitance of the electrode increased to 112.9% of its initial value from the first cycle to 2100 cycles which indicates the enhanced energy retention properties. From ~2100 cycles, there is gradual and stable decrease in specific capacitance since it reduced to 22.2% of its initial value after 10 000 cycles showing the cyclic stability of the device. The reasons for

the gradual decrease in specific capacitance might be due to the voltage drop in the electrode, electrolyte precipitation over the course of time, change in concentration, and ionic conductivity of the electrolyte.

3.7 | Solid state flexible supercapacitor

The electrochemical performance of the Exf. ACHS (1:3, 900, 2) coated stainless steel mesh electrodes were further investigated in two electrode configuration using hydroxyethyl cellulose /Na_2SO_4 biopolymer electrolyte which provides an operating potential window of 1.6 V (0 to 1.6 V). Figure 8A shows two CVs, one cycled from −0.8 to 1.6 V and the second is the same device cycled from 0 to 1.6 V at 25 mV s^{-1} scan rate. When a device is cycled from negative to positive potential, there are increased current levels due to the reversing the polarity of the device. For activated carbon based symmetric supercapacitor devices, the capacitive nature of the device generally relies on the rectangular shaped CV curve within a specified potential window. In our present study, we observed

that the CV curve remained rectangular in shape within −0.8 to 1.6 V (negative to positive potential window) and also between 0 to 1.6 V (positive potential window) range. But in general, both the symmetric/asymmetric supercapacitor devices should never be tested in negative potential window because by doing so we are reversing the polarity of the devices which severely impacts the structural stability of the electrodes.[103] Hence, it is always advisable to test the devices with the potential starting from zero and this particular study, the device is scanned between 0 to 1.6 V potential window. As shown in Figure 8B, the CV showed rectangular shaped curve at 5 mV s^{-1} indicating ideal double layer capacitance is formed at lower scan rates. Moreover, there is little deviation in its capacitive behavior at higher scan rates showing good rate capability of the device. As shown in Figure 8C, no obvious change in its double layer behavior is observed when the CV was performed over extended potential windows (from 0.8 to 1.6 V) indicating the stability of the device over different operating voltage ranges. Figure 8D shows the Nyquist plot of Exf. ACHS (1:3, 900, 2) symmetric device along with its equivalent
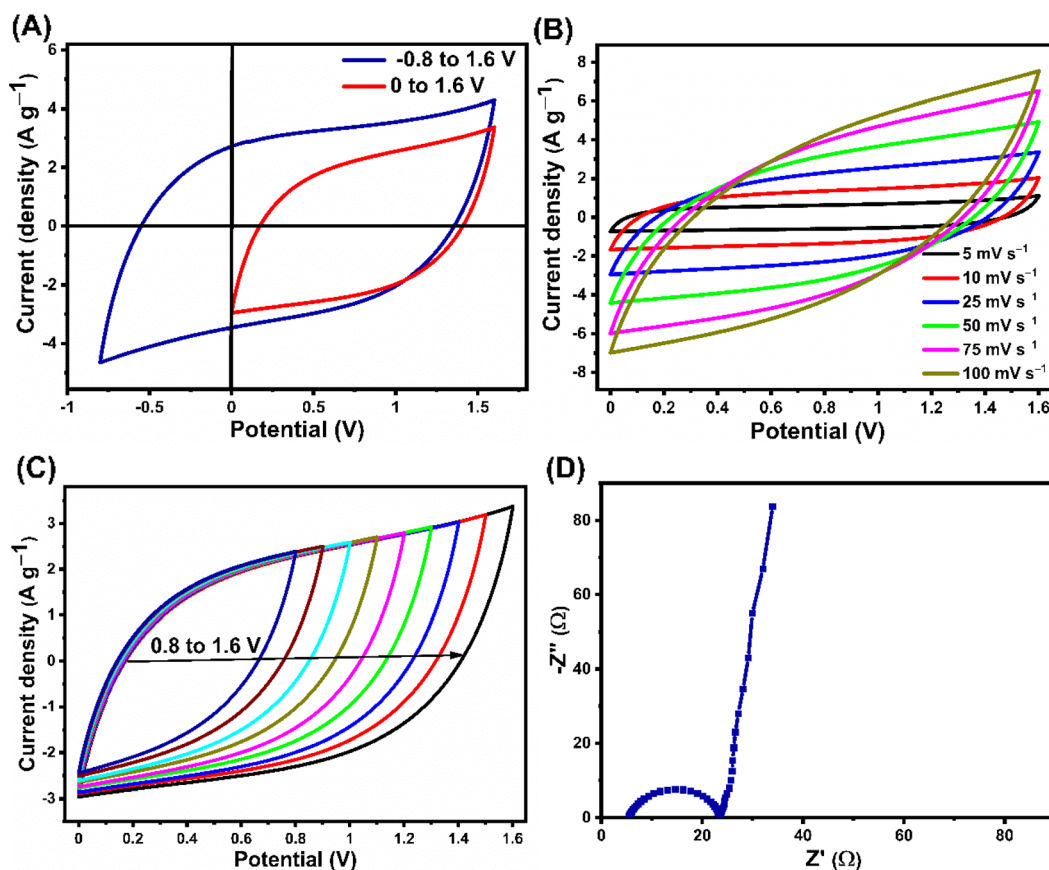

FIGURE 8 (A) Cyclic Voltammetrys (CVs) from −0.8 to 1.6 V and 0 to 1.6 V at 25 mV s^{-1} (B) CV plot at different scan rates (C) CV plot at different potential windows (D) Nyquist plot of flexible supercapacitor device with sono-exfoliated graphene-like activated carbon [Exf. ACHS (1:3, 900, 2)] coated stainless steel electrodes and HEC/Na_2SO_4 bio-polymer electrolyte

circuit model. The series resistance (Rs) of the device is 17.9 Ω which is the sum of electronic and ionic resistance of two electrodes, electrolytes, and also the electrical contacts used in the measurement. The diameter of the small semicircle in between high to medium frequency region gives the charge transfer resistance (Rct) of the gel electrolyte ions inside the activated carbon framework. The charge transfer resistance is found to be 4.4 Ω, indicating the smooth ionic transport kinetics within the carbon pores. A nearly vertical straight line is observed in the low frequency region indicating the capacitive characteristics of the device.

The GCD curves shown in Figure 9A demonstrated good symmetry and linear charge/discharge profiles within 0 to 1.6 V which indicates instantaneous formation of double-layer and effective ionic diffusion within the electrode. From GCD curves, the total capacitance C_t of the device at various current densities was calculated

according to Equation (5). It was observed that at lower current density of 0.25 A g^{-1} a total capacitance of 101.7 F g^{-1} is obtained but at higher current density, capacitance in HEC/Na_2SO_4 electrolyte dropped to 37.5 F g^{-1}, that is, a 36.8% retention in capacitance when the current density was increased to 30 A g^{-1}, exhibiting an outstanding rate capability. The GCD curves shown in Figure 9B display linear charge discharge behavior over wide potential ranges indicating the capability of the device to exhibit a double layer mechanism. Figure 9C shows the dependence of energy density on the potential window. At lower potentials, the full capacity of the device is not utilized properly. But at higher potentials, the device is charged to its full capacity leading to a higher discharge time and an increase in energy density. Figure 9D shows the electrochemical cyclic stability of the flexible supercapacitor device performed over 10 000 cycles [ran continuously for 12 days] at 5 A g^{-1}
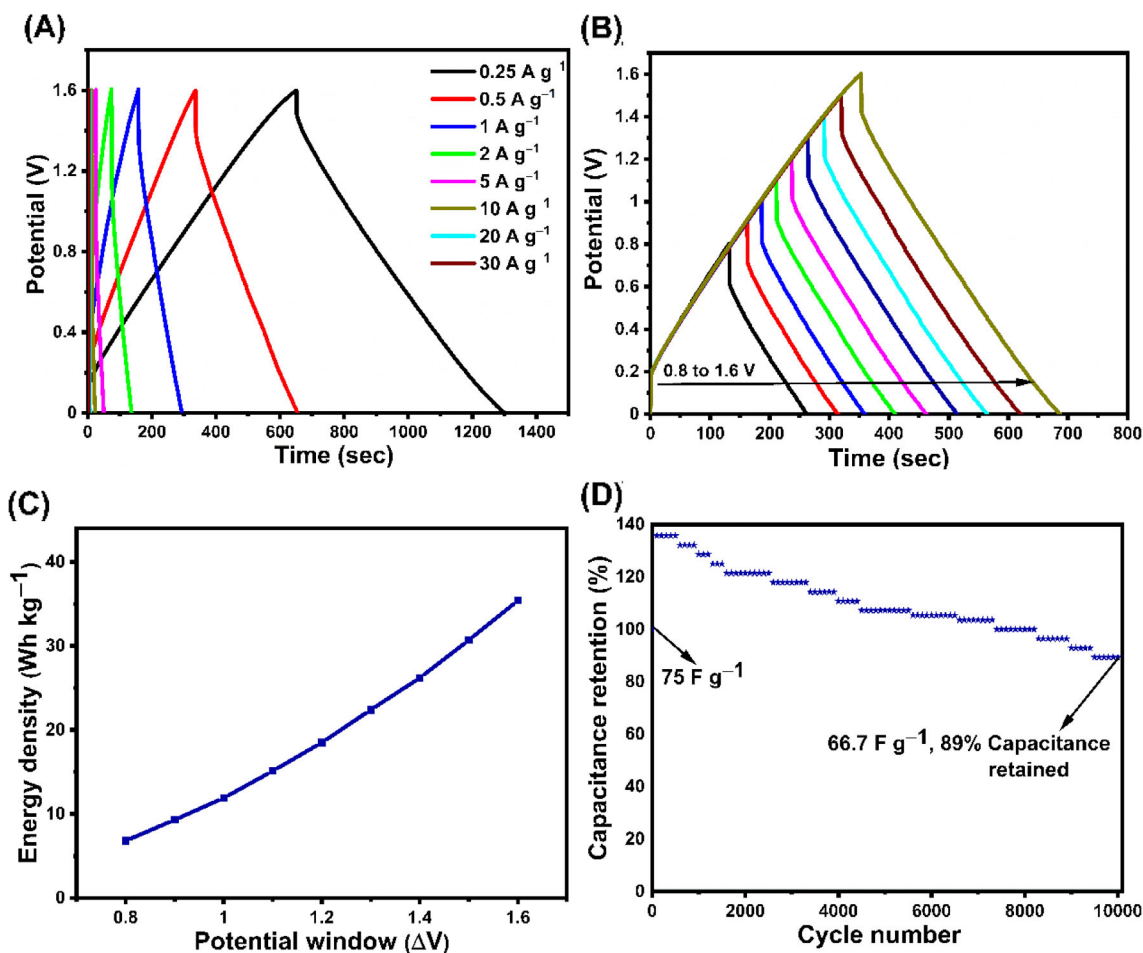
FIGURE 9 (A) Galvanostatic charge-discharge (GCD) plots at different current densities (B) GCD graphs under different potential windows at 0.5 A g^{-1} current density (C) Dependence of Energy density on potential window at 0.5 A g^{-1} current density of flexible supercapacitor device with sono-exfoliated graphene-like activated carbon Exf. ACHS (1:3, 900, 2) and HEC/Na_2SO_4 bio-polymer electrolyte (D) Cyclic stability profile of flexible supercapacitor device with sono-exfoliated activated carbon Exf. ACHS (1:3, 900, 2) and HEC/Na_2SO_4 bio-polymer electrolyte over 10 000 cycles at 5 A g^{-1}

current density. The capacitance of the device progressively increased during the first 1000 cycles with a 135.7% increase in its capacitance and it then reduced gradually and steadily thereafter, reaching 89% after 10 000 cycles. The reason for the increase can be attributed to the complete utilization of all the porous carbon framework by the bio-polymer gel electrolyte whereas the decrease might be attributed to the graphene-like structures in the porous carbon framework which tend to stack during continuous charge discharge cycles. A Ragone plot of Exf. ACHS (1:3, 900, 2)-based flexible supercapacitor device with HEC/Na_2SO_4 bio-polymer electrolyte [calculated from the discharge curves using Equations (7 and 8)]
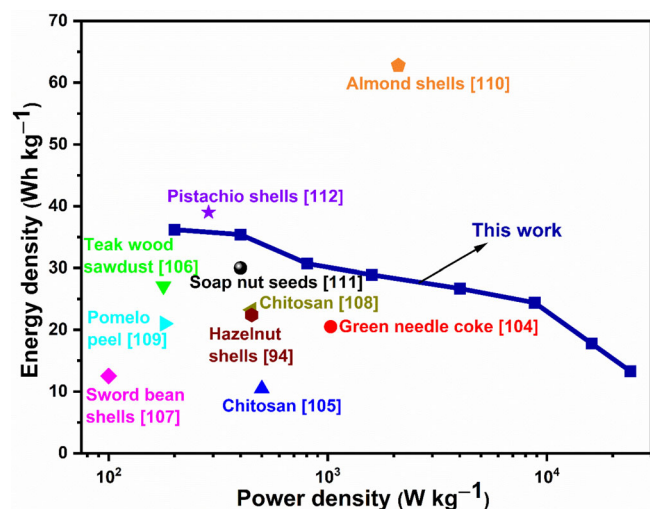

FIGURE 10 Ragone plot of Exf. ACHS (1:3, 900, 2)-based flexible supercapacitor device compared biomass-derived supercapacitors reported recently in literature

along with the data for bio-mass derived supercapacitor devices recently reported in literature are shown in Figure 10. Benefiting from the wider operating potential (1.6 V) and high specific capacitance, the bio-polymeric based flexible supercapacitor exhibits a high energy density of 36.2 Wh kg^{-1} at power densities of 199.7 W kg^{-1}. Owing to its good rate capability, at current density of 30 Ag^{-1}, the flexible device still secured energy density of 13.3 Wh kg^{-1} even at higher power densities of 24 000 W kg^{-1} which is an attractive result and competitive to most recently reported devices with nut-shells and other biomass carbon electrodes.[94,104-112] The reason behind this excellent performance is attributed to the graphene-like porous carbons with high surface area obtained through sono-exfoliation process promoting faster ion-transport kinetics with high energy storage capability making them an ideal choice for supercapacitor electrodes. To further demonstrate the mechanical stability of the Exf. ACHS (1:3, 900, 2) based symmetric flexible supercapacitor for practical application, CV was performed on the device at different bending radius. As shown in Figure 11A, the device can be mechanically bent without sacrificing its structural integrity. Particularly, the device can withstand different bending positions(as shown in inset of Figure 11A) thereby endowing them with great potential for practical applications. Figure 11A depicts the CV curves of *symmetrical device* under various bending radius, demonstrating that the electrochemical performance of the device remained almost unchanged under mechanical bending. These results show that the fabricated device possess excellent stability and mechanical flexibility. In order to study the commercial application and performance of the
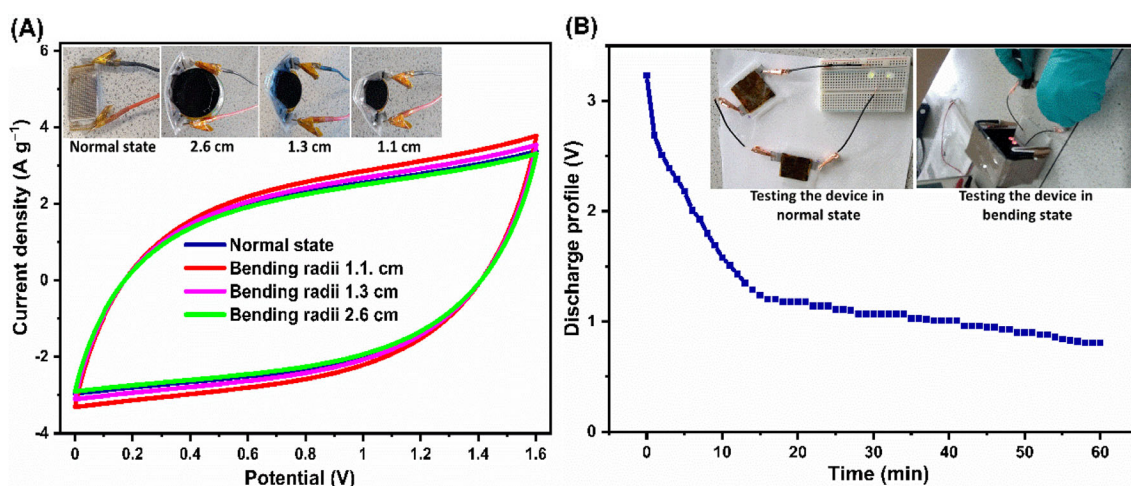

FIGURE 11 (A) Cyclic Voltammetry curves of flexible supercapacitor at different bending diameters. Inset shows the photographs of the device attached to three vials of different diameters (B) Discharge profile of two devices connected in series. Inset displays the photograph of two flexible supercapacitor devices connected in series powering two LEDs under normal state and bending state

developed device, two symmetrical flexible supercapacitors were connected in series and two light emitting diodes (LEDs) were connected in parallel were used to discharge the device (inset of Figure 11B). After charging the device using a constant DC power supply (3.2 V) for 60 s, the discharge profile was monitored as a function of time (Figure 11B). A discharge voltage of 2.69 V [0.51 V voltage drop] was observed which was monitored for 3600 s. For the first 960 s, the discharge-profile remained linear which is in accordance with the carbon-based double layer device characteristics. After 600 s, the discharge voltage dropped below 1.6 V and the devices were unable to power the LEDs as the minimum voltage required to power them is 1.6 V. From ∼1200 s onwards, there is a gradual drop in potential and since the LEDs are not accepting any power, the supercapacitors maintained 0.81 V even after 3600 s (1 h). These results infer that the fabricated devices with sono-exfoliated graphene-like activated carbon coated stainless steel electrode and bio-polymer electrolyte exhibits significant potential for energy storage applications.

4 | CONCLUSIONS

Multi-layered graphene-like activated carbon were produced using simple sono-exfoliation of the chemically activated carbon derived from hazelnut shells and used as electrodes for symmetric flexible supercapacitor using hydroxyethyl cellulose based bio-polymer electrolyte. The structural and morphological analysis revealed the presence of graphene-like features embedded in a porous carbon framework. Spectroscopy studies revealed that the sono-exfoliated carbon has lower degree of defects compared to the chemically activated sample before sono-exfoliation. Electrochemical tests in 1 M Na_2SO_4 aqueous electrolyte revealed that the multi-layered graphene-like activated carbon exhibited highest specific capacitance with retention of 46.7% at 30 A g^{-1} current density, indicating the high rate capability of the electrode material. Also, graphene-like activated carbon showed a high-power density of 14 976 W kg^{-1} corresponding to a high energy density of 20.83 W kg^{-1} with outstanding capacitance retention of 77.8% even after 10 000 charge/discharge cycles repeated over 19 days continuously in aqueous electrolyte. Most importantly, the assembled flexible symmetric supercapacitor device with graphene-like activated carbon can successfully operate within an extended potential window of 0 to 1.6 V and offered high energy density of 36.2 Wh kg^{-1} at power densities of 199.7 W kg^{-1}. Moreover, the device displayed excellent flexibility over different bending radii and illuminated two green LEDs (connected in parallel) via discharging two symmetric flexible supercapacitors connected in series. This study demonstrates the potential of a simple sono-exfoliation strategy to produce high performance graphene-like carbon electrode material and the use of bio-polymer electrolyte for developing flexible, portable, and mechanically robust supercapacitor device using a low cost, scalable, and eco-benign approach in order to meet the energy requirements of flexible and wearable electronics.

DATA AVAILABILITY STATEMENT
The data that support the findings of this study are available from the corresponding author upon reasonable request.

ORCID
Aruna Ivaturi https://orcid.org/0000-0003-0485-6570

REFERENCES
1. Herou S, Schlee P, Jorge AB, Titirici M. Biomass-derived electrodes for flexible supercapacitors. *Curr Opin Green Sustain Chem.* 2018;9:18-24.
2. Guan L, Pan L, Peng T, et al. Synthesis of biomass-derived nitrogen-doped porous carbon nanosheets for high-performance supercapacitors. *ACS Sustain Chem Eng.* 2019; 7(9):8405-8412.

3. Borenstein A, Hanna O, Attias R, Luski S, Brousse T, Aurbach D. Carbon-based composite materials for supercapacitor electrodes: a review. *J Mater Chem A*. 2017;5(25):12653-12672.

4. He D, Huang Z-H, Wang M-X. Porous nitrogen and oxygen co-doped carbon microtubes derived from plane tree fruit fluff for high-performance supercapacitors. *J Mater Sci Mater Electron*. 2019;30(2):1468-1479.

5. Zhang J, Jin L, Cheng J, Hu H. Hierarchical porous carbons prepared from direct coal liquefaction residue and coal for supercapacitor electrodes. *Carbon*. 2013;55:221-232.

6. Li M, Xiao H, Zhang T, Li Q, Zhao Y. Activated carbon fiber derived from sisal with large specific surface area for high-performance supercapacitors. *ACS Sustain Chem Eng*. 2019; 7(5):4716-4723.

7. Dos Reis GS, Larsson SH, de Oliveira HP, Thyrel M, Claudio LE. Sustainable biomass activated carbons as electrodes for battery and supercapacitors—a mini-review. *Nanomaterials*. 2020;10(7):1398.

8. Liu Y, Chen J, Cui B, Yin P, Zhang C. Design and preparation of biomass-derived carbon materials for supercapacitors: a review. *C*. 2018;4(4):53.

9. Jiang L, Sheng L, Fan Z. Biomass-derived carbon materials with structural diversities and their applications in energy storage. *Sci China Mater*. 2018;61(2):133-158.

10. Mi J, Wang X-R, Fan R-J, Qu W-H, Li W-C. Coconut-shell-based porous carbons with a tunable micro/mesopore ratio for high-performance supercapacitors. *Energy Fuel*. 2012; 26(8):5321-5329.

11. Fahmi F, Dewayanti NAA, Widiyastuti W, Setyawan H. Preparation of porous graphene-like material from coconut shell charcoals for supercapacitors. *Cogent Eng*. 2020;7(1):1748962.

12. Misnon II, Zain NKM, Jose R. Conversion of oil palm kernel shell biomass to activated carbon for supercapacitor electrode application. *Waste Biomass Valoriz*. 2019;10(6):1731-1740.

13. Purkait T, Singh G, Singh M, Kumar D, Dey RS. Large area few-layer graphene with scalable preparation from waste biomass for high-performance supercapacitor. *Sci Rep*. 2017;7(1):1-14.

14. Wu M-F, Hsiao C-H, Lee C-Y, Tai N-H. Flexible supercapacitors prepared using the peanut-shell-based carbon. *ACS Omega*. 2020;5(24):14417-14426.

15. Xu X, Gao J, Tian Q, Zhai X, Liu Y. Walnut shell derived porous carbon for a symmetric all-solid-state supercapacitor. *Appl Surf Sci*. 2017;411:170-176.

16. Lu X, Xiang K, Zhou W, Zhu Y, Chen H. Biomass carbon materials derived from macadamia nut shells for high-performance supercapacitors. *Bull Mater Sci*. 2018;41(6):1-7.

17. Faisal MSS, Abedin F, Asmatulu R. Activated carbons of pistachio and acorn shells for supercapacitor electrodes with TEABF$_4$/PC solutions as electrolytes. *Carbon Lett*. 2020;30(5):509-520.

18. Wartelle LH, Marshall WE. Nutshells as granular activated carbons: physical, chemical and adsorptive properties. *J Chem Technol Biotechnol Int Res Process Env Clean Technol*. 2001; 76(5):451-455.

19. Pütün AE, Özcan A, Pütün E. Pyrolysis of hazelnut shells in a fixed-bed tubular reactor: yields and structural analysis of bio-oil. *J Anal Appl Pyrolysis*. 1999;52(1):33-49.

20. Recepoğlu YK, Yüksel A. Phosphorylated hazelnut shell waste for sustainable lithium recovery application as biosorbent. *Cellul*. 2021;28(15):9837-9855.

21. Liu S, Ma R, Hu X, et al. CO2 adsorption on hazelnut-shell-derived nitrogen-doped porous carbons synthesized by single-step sodium amide activation. *Ind Eng Chem Res*. 2019;59(15):7046-7053.

22. Milenković D, Dašić P, Veljković V. Ultrasound-assisted adsorption of copper (II) ions on hazelnut shell activated carbon. *Ultrason Sonochem*. 2009;16(4):557-563.

23. Daud WMAW, Ali WSW. Comparison on pore development of activated carbon produced from palm shell and coconut shell. *Bioresour Technol*. 2004;93(1):63-69.

24. Bharthare P, Shrivastava P, Singh P, Ttiwari A. Peanut shell as renewable energy source and their utility in production of ethanol. *Int J Adv Res*. 2014;2:1-12.

25. Uzuner S, Cekmecelioglu D. A rapid screening approach to factors affecting dilute acid hydrolysis of hazelnut shells. *Int Proceed Chem Biol Env Eng*. 2013;50:180-185.

26. Pirayesh H, Khazaeian A, Tabarsa T. The potential for using walnut (Juglans regia L.) shell as a raw material for wood-based particleboard manufacturing. *Compos Part B Eng*. 2012; 43(8):3276-3280.

27. Li X, Liu Y, Hao J, Wang W. Study of almond Shell characteristics. *Study Almond Shell Charact Mater*. 2018;11(9):1782.

28. Nuithitikul K, Phromrak R, Saengngoen W. Utilization of chemically treated cashew-nut shell as potential adsorbent for removal of Pb (II) ions from aqueous solution. *Sci Rep*. 2020; 10(1):1-14.

29. Wechsler A, Zaharia M, Crosky A, et al. Macadamia (Macadamia integrifolia) shell and castor (Rícinos communis) oil based sustainable particleboard: a comparison of its properties with conventional wood based particleboard. *Mater Design*. 2013;50:117-123.

30. Wang J, Zhang X, Li Z, Ma Y, Ma L. Recent progress of biomass-derived carbon materials for supercapacitors. *J Power Sources*. 2020;451:227794.

31. Gürünlü B, Taşdelen-Yücedağ Ç, Bayramoğlu M. Graphene synthesis by ultrasound energy-assisted exfoliation of graphite in various solvents. *Crystals*. 2020;10(11):1037.

32. Lin Z, Karthik PS, Hada M, Nishikawa T, Hayashi Y. Simple technique of exfoliation and dispersion of multilayer graphene from natural graphite by ozone-assisted sonication. *Nanomaterials*. 2017;7(6):125.

33. Alipoori S, Mazinani S, Aboutalebi SH, Sharif F. Review of PVA-based gel polymer electrolytes in flexible solid-state supercapacitors: opportunities and challenges. *J Energy Stor*. 2020;27:101072.

34. Ye T, Li L, Zhang Y. Recent progress in solid electrolytes for energy storage devices. *Adv Funct Mater*. 2020;30(29):2000077.

35. Pal B, Yang S, Ramesh S, Thangadurai V, Jose R. Electrolyte selection for supercapacitive devices: a critical review. *Nanoscale Adv*. 2019;1(10):3807-3835.

36. Dai H, Zhang G, Rawach D, et al. Polymer gel electrolytes for flexible supercapacitors: recent progress, challenges, and perspectives. *Energy Stor Mater*. 2021;34:320-355.

37. Ghasemi M, Fahimi Z, Moradlou O, Sovizi MR. Porous gel polymer electrolyte for the solid state metal oxide supercapacitor with a wide potential window. *J Taiwan Inst Chem Eng*. 2021;118:223-231.

38. Jian M, Zhang Y, Liu Z. Natural biopolymers for flexible sensing and energy devices. *Chinese J Polymer Sci.* 2020;38(5):459-490.

39. Sun Z, Zheng M, Hu H, et al. From biomass wastes to vertically aligned graphene nanosheet arrays: a catalyst-free synthetic strategy towards high-quality graphene for electrochemical energy storage. *Chem Eng J.* 2018;336:550-561.

40. Sevilla M, Fuertes AB. A green approach to high-performance supercapacitor electrodes: the chemical activation of hydrochar with potassium bicarbonate. *ChemSusChem.* 2016;9(14):1880-1888.

41. Sun L, Park SS, Sheberla D, Dincă M. Measuring and reporting electrical conductivity in metal–organic frameworks: Cd_2 (TTFTB) as a case study. *J Am Chem Soc.* 2016;138(44):14772-14782.

42. Cai N, Cheng H, Jin H, Liu H, Zhang P, Wang M. Porous carbon derived from cashew nut husk biomass waste for high-performance supercapacitors. *J Electroanal Chem.* 2020;861:113933.

43. Yang G, Park S-J. Nanoflower-like NiCo2O4 grown on biomass carbon coated nickel foam for asymmetric supercapacitor. *J Alloys Compd.* 2020;835:155270.

44. Yang H, Zhou J, Wang M, Wu S, Yang W, Wang H. From basil seed to flexible supercapacitors: Green synthesis of heteroatom-enriched porous carbon by self-gelation strategy. *Int J Energy Res.* 2020;44(6):4449-4463.

45. Gozaydin G, Yuksel A. Valorization of hazelnut shell waste in hot compressed water. *Fuel Process Technol.* 2017;166:96-106.

46. Díez D, Urueña A, Piñero R, Barrio A, Tamminen T. Determination of hemicellulose, cellulose, and lignin content in different types of biomasses by thermogravimetric analysis and pseudocomponent kinetic model (TGA-PKM method). *Processes.* 2020;8(9):1048.

47. Zhu L, Zhong Z. Effects of cellulose, hemicellulose and lignin on biomass pyrolysis kinetics. *Korean J Chem Eng.* 2020;37(10):1660-1668.

48. Wang J, Kaskel S. KOH activation of carbon-based materials for energy storage. *J Mater Chem.* 2012;22(45):23710-23725.

49. Long C, Chen X, Jiang L, Zhi L, Fan Z. Porous layer-stacking carbon derived from in-built template in biomass for high volumetric performance supercapacitors. *Nano Energy.* 2015;12:141-151.

50. Fang K, Yang R. A comparison on the efficiency of raw activated carbon, oxidized, and sulfurized adsorbents for furfural adsorption. *Alex Eng J.* 2021;60(1):1241-1248.

51. Demiral H, Demiral I, Tümsek F, Karabacakoğlu B. Pore structure of activated carbon prepared from hazelnut bagasse by chemical activation. *Surface Interf Anal Int J Devot Develop Appl Techn Analy Surfaces Interfaces Thin Films.* 2008;40(3–4):616-619.

52. Lin Y, Chen Z, Yu C, Zhong W. Facile synthesis of high nitrogen-doped content, mesopore-dominated biomass-derived hierarchical porous graphitic carbon for high performance supercapacitors. *Electrochim Acta.* 2020;334:135615.

53. Morton JA, Khavari M, Qin L, et al. New insights into sono-exfoliation mechanisms of graphite: in situ high-speed imaging studies and acoustic measurements. *Mater Today.* 2021;49:10-22.

54. Wang Y, Yang R, Wei Y, Zhao Z, Li M. Preparation of novel pigskin-derived carbon sheets and their low-temperature activation-induced high capacitive performance. *RSC Adv.* 2014;4(85):45318-45324.

55. Hu S-C, Cheng J, Wang W-P, et al. Structural changes and electrochemical properties of lacquer wood activated carbon prepared by phosphoric acid-chemical activation for supercapacitor applications. *Renew Energy.* 2021;177:82-94.

56. Mohamedkhair AK, Aziz MA, Shah SS, et al. Effect of an activating agent on the physicochemical properties and supercapacitor performance of naturally nitrogen-enriched carbon derived from Albizia procera leaves. *Arabian J Chem.* 2020;13(7):6161-6173.

57. Nie Z, Huang Y, Ma B, et al. Nitrogen-doped carbon with modulated surface chemistry and porous structure by a stepwise biomass activation process towards enhanced electrochemical lithium-ion storage. *Sci Rep.* 2019;9(1):1-9.

58. Achee TC, Sun W, Hope JT, et al. High-yield scalable graphene nanosheet production from compressed graphite using electrochemical exfoliation. *Sci Rep.* 2018;8(1):1-8.

59. Hu M, Yao Z, Wang X. Characterization techniques for graphene-based materials in catalysis. *AIMS Mater Sci.* 2017;4(3):755-788.

60. Wall M. The Raman spectroscopy of graphene and the determination of layer thickness. *Thermo Sci.* 2011;5:1-5.

61. Tang B, Guoxin H, Gao H. Raman spectroscopic characterization of graphene. *Appl Spectrosc Rev.* 2010;45(5):369-407.

62. Momodu D, Madito M, Barzegar F, et al. Activated carbon derived from tree bark biomass with promising material properties for supercapacitors. *J Solid State Electrochem.* 2017;21(3):859-872.

63. Jawhari T, Roid A, Casado J. Raman spectroscopic characterization of some commercially available carbon black materials. *Carbon.* 1995;33(11):1561-1565.

64. Bedia J, Peñas-Garzón M, Gómez-Avilés A, Rodriguez JJ, Belver C. Review on activated carbons by chemical activation with $FeCl_3$. *C.* 2020;6(2):21.

65. Gunasekaran SS, Elumalali SK, Kumaresan TK, et al. Partially graphitic nanoporous activated carbon prepared from biomass for supercapacitor application. *Mater Lett.* 2018;218:165-168.

66. Kalita G, Wakita K, Umeno M. Low temperature growth of graphene film by microwave assisted surface wave plasma CVD for transparent electrode application. *RSC Adv.* 2012;2(7):2815-2820.

67. Wu X, Tian Z, Hu L, Huang S, Cai J. Macroalgae-derived nitrogen-doped hierarchical porous carbons with high performance for H 2 storage and supercapacitors. *RSC Adv.* 2017;7(52):32795-32805.

68. Chen H, Yu F, Wang G, Chen L, Dai B, Peng S. Nitrogen and sulfur self-doped activated carbon directly derived from elm flower for high-performance supercapacitors. *ACS Omega.* 2018;3(4):4724-4732.

69. Huang Y, Zhao G. Preparation and characterization of activated carbon fibers from liquefied wood by KOH activation. *Holzforschung.* 2016;70(3):195-202.

70. Lee M-S, Park M, Kim HY, Park S-J. Effects of microporosity and surface chemistry on separation performances of N-containing pitch-based activated carbons for CO_2/N_2 binary mixture. *Sci Rep.* 2016;6(1):1-11.

71. Smith M, Scudiero L, Espinal J, McEwen J-S, Garcia-Perez M. Improving the deconvolution and interpretation of XPS spectra from chars by ab initio calculations. *Carbon*. 2016;110: 155-171.

72. Chen R, Li L, Liu Z, et al. Preparation and characterization of activated carbons from tobacco stem by chemical activation. *J Air Waste Manage Assoc*. 2017;67(6):713-724.

73. Mutuma BK, Matsoso BJ, Momodu D, Oyedotun KO, Coville NJ, Manyala N. Deciphering the structural, textural, and electrochemical properties of activated BN-doped spherical carbons. *Nanomaterials*. 2019;9(3):446.

74. Wu Y, Fang S, Jiang Y. Effects of nitrogen on the carbon anode of a lithium secondary battery. *Solid State Ion*. 1999; 120(1–4):117-123.

75. Ilnicka A, Skorupska M, Szkoda M, et al. Combined effect of nitrogen-doped functional groups and porosity of porous carbons on electrochemical performance of supercapacitors. *Sci Rep*. 2021;11(1):1-11.

76. Sattayarut V, Wanchaem T, Ukkakimapan P, et al. Nitrogen self-doped activated carbons via the direct activation of Samanea saman leaves for high energy density supercapacitors. *RSC Adv*. 2019;9(38):21724-21732.

77. Gu X, Zhao Y, Sun K, et al. Method of ultrasound-assisted liquid-phase exfoliation to prepare graphene. *Ultrason Sonochem*. 2019;58:104630.

78. Muthoosamy K, Manickam S. State of the art and recent advances in the ultrasound-assisted synthesis, exfoliation and functionalization of graphene derivatives. *Ultrason Sonochem*. 2017;39:478-493.

79. Yin W-M, Tian L-F, Pang B, Guo Y-R, Li S-J, Pan Q-J. Fabrication of dually N/S-doped carbon from biomass lignin: porous architecture and high-rate performance as supercapacitor. *Int J Biol Macromol*. 2020;156:988-996.

80. Mishra R, Prasad PR, Panda P, Barman S. Highly porous activated N-doped carbon as an ideal electrode material for capacitive energy storage and Physisorption of H_2, CO_2, and CH4. *Energy Fuel*. 2021;35(17):14177-14187.

81. Mirzaeian M, Abbas Q, Hunt M, Hall P. Pseudocapacitive effect of carbons doped with different functional groups as electrode materials for electrochemical capacitors. *Energies*. 2020;13(21):5577.

82. Lee J-SM, Briggs ME, Hu C-C, Cooper AI. Controlling electric double-layer capacitance and pseudocapacitance in heteroatom-doped carbons derived from hypercrosslinked microporous polymers. *Nano Energy*. 2018;46:277-289.

83. Qin C, Wang S, Wang Z, et al. Hierarchical porous carbon derived from Gardenia jasminoides Ellis flowers for high performance supercapacitor. *J Energy Stor*. 2021;33:102061.

84. Gandla D, Wu X, Zhang F, Wu C, Tan DQ. High-performance and high-voltage supercapacitors based on N-doped mesoporous activated carbon derived from dragon fruit peels. *ACS Omega*. 2021;6(11):7615-7625.

85. Zhong G, Xu S, Chao J, et al. Biomass-derived nitrogen-doped porous carbons activated by magnesium chloride as ultrahigh-performance Supercapacitors. *Ind Eng Chem Res*. 2020;59(50): 21756-21767.

86. Hsiao C, Lee C, Tai N. Biomass-derived three-dimensional carbon framework for a flexible fibrous supercapacitor and its application as a wearable smart textile. *RSC Adv*. 2020;10(12): 6960-6972.

87. Manjakkal L, Pullanchiyodan A, Yogeswaran N, Hosseini ES, Dahiya R. A wearable supercapacitor based on conductive PEDOT: PSS-coated cloth and a sweat electrolyte. *Adv Mater*. 2020;32(24):1907254.

88. Liu Z, Hu J, Shen F, et al. Trichoderma bridges waste biomass and ultra-high specific surface area carbon to achieve a high-performance supercapacitor. *J Power Sources*. 2021;497:229880.

89. Januszewicz K, Cymann-Sachajdak A, Kazimierski P, Klein M, Łuczak J, Wilamowska-Zawłocka M. Chestnut-derived activated carbon as a prospective material for energy storage. *Materials*. 2020;13(20):4658.

90. Jiang M, Zhang J, Xing L, et al. KOH-activated porous carbons derived from chestnut Shell with superior capacitive performance. *Chinese J Chem*. 2016;34(11):1093-1102.

91. Lee K-C, Lim MSW, Hong Z-Y, et al. Coconut shell-derived activated carbon for high-performance solid-state supercapacitors. *Energies*. 2021;14(15):4546.

92. Sun L, Tian C, Li M, et al. From coconut shell to porous graphene-like nanosheets for high-power supercapacitors. *J Mater Chem A*. 2013;1(21):6462-6470.

93. Xie Y, Zhang D, Jati GNP, et al. Effect of structural and compositional alterations on the specific capacitance of hazelnut shell activated carbon. *Colloids Surf A Physicochem Eng Asp*. 2021;625:126951.

94. Liu Y, Liu P, Li L, et al. Fabrication of biomass-derived activated carbon with interconnected hierarchical architecture via H_3PO_4-assisted KOH activation for high-performance symmetrical supercapacitors. *J Electroanal Chem*. 2021;903: 115828.

95. Zhang J, Chen H, Bai J, et al. N-doped hierarchically porous carbon derived from grape marcs for high-performance supercapacitors. *J Alloys Compd*. 2021;854:157207.

96. Merin P, Jimmy Joy P, Muralidharan M, Veena Gopalan E, Seema A. Biomass-derived activated carbon for high-performance Supercapacitor electrode applications. *Chem Eng Technol*. 2021;44(5):844-851.

97. Yan X, Jia Y, Zhuang L, Zhang L, Wang K, Yao X. Defective carbons derived from macadamia nut shell biomass for efficient oxygen reduction and supercapacitors. *ChemElectroChem*. 2018;5(14):1874-1879.

98. Sodtipinta J, Amornsakchai T, Pakawatpanurut P. Nanoporous carbon derived from agro-waste pineapple leaves for supercapacitor electrode. *Adv Nat Sci Nanosci Nanotechnol*. 2017;8(3):035017.

99. Park MH, Yun YS, Cho SY, Kim NR, Jin H-J. Waste coffee grounds-derived nanoporous carbon nanosheets for supercapacitors. *Carbon Lett*. 2016;19:66-71.

100. Natalia M, Sudhakar Y, Selvakumar M. Activated carbon derived from natural sources and electrochemical capacitance of double layer capacitor. 2013.

101. Subramanian V, Luo C, Stephan AM, Nahm K, Thomas S, Wei B. Supercapacitors from activated carbon derived from banana fibers. *J Phys Chem C*. 2007;111(20):7527-7531.

102. Guo F, Jiang X, Li X, Peng K, Guo C, Rao Z. Carbon electrode material from peanut shell by one-step synthesis for high performance supercapacitor. *J Mater Sci Mater Electron*. 2019; 30(1):914-925.

103. Stoller MD, Ruoff RS. Best practice methods for determining an electrode material's performance for ultracapacitors. *Energ Environ Sci*. 2010;3(9):1294-1301.

104. Cheng J, Lu Z, Zhao X, Chen X, Liu Y. Green needle coke-derived porous carbon for high-performance symmetric supercapacitor. *J Power Sources*. 2021;494:229770.

105. Chen K, Weng S, Lu J, et al. Facile synthesis of chitosan derived heteroatoms-doped hierarchical porous carbon for supercapacitors. *Microporous Mesoporous Mater*. 2021;320: 111106.

106. Bhat VS, Krishnan SG, Jayeoye TJ, et al. Self-activated 'green'-carbon nanoparticles for symmetric solid-state supercapacitors. *J Mater Sci*. 2021;56(23):13271-13290.

107. Chen T, Luo L, Luo L, et al. High energy density supercapacitors with hierarchical nitrogen-doped porous carbon as active material obtained from bio-waste. *Renew Energy*. 2021;175:760-769.

108. Qiao Y, Zhang R, Li R, Fang W, Cui Z, Zhang D. Green preparation of hierarchical porous carbon with tunable pore size for supercapacitors. *Ionics*. 2021;27(7):3077-3087.

109. Wang Z, Zheng P, Guo J. Pomelo peel-derived lamellar carbon with surface oxygen functional groups for high-performance supercapacitors. *Appl Phys A*. 2021;127(5):1-9.

110. Jain A, Tripathi S. Almond shell-based activated nanoporous carbon electrode for EDLCs. *Ionics*. 2015;21(5):1391-1398.

111. Vinayagam M, Suresh Babu R, Sivasamy A, de Barros ALF. Biomass-derived porous activated carbon nanofibers from Sapindus trifoliatus nut shells for high-performance symmetric supercapacitor applications. *Carbon Lett*. 2021;31(6):1133-1143.

112. Xu J, Gao Q, Zhang Y, et al. Preparing two-dimensional microporous carbon from pistachio nutshell with high areal capacitance as supercapacitor materials. *Sci Rep*. 2014;4(1): 1-6.

SUPPORTING INFORMATION

Additional supporting information can be found online in the Supporting Information section at the end of this article.